University of Alberta

Modeling Cavitation in a High Intensity Agitation Cell

by

July Kooran Jose

A thesis submitted to the Faculty of Graduate Studies and Research
in partial fulfillment of the requirements for the degree of

Master of Science

in

Chemical Engineering

Department of Chemical and Materials Engineering

Spring 2011
Edmonton, Alberta

Abstract

The presence of hydrodynamically generated air bubbles has been observed to enhance fine particle flotation in a high intensity agitation (HIA) flotation cell. In this study, the cavitation in an HIA cell, used in our laboratory, is studied by hydrodynamic computational fluid dynamics. Different types of impellers are studied to obtain flow characteristics such as velocity and pressure distributions and turbulent dissipation rate in a two-baffled HIA cell. A cavitation model in conjunction with a multiphase mixture model is used to predict the vapor generation in the HIA cell. Cavitating flow is simulated as a function of revolution speed (RPM) and dissolved gas concentration to understand the dependency of hydrodynamic cavitation on these operating parameters. For comparison, cavitation in a pressure driven flow through a constriction is also modeled. A population balance model is used to obtain bubble size distributions of the generated cavities in a flow through constriction.

Acknowledgments

I would like to express my sincerest appreciation to:

My supervisors Dr. Zhenghe Xu, Dr. Robert Hayes and Dr. Joe Mmbaga for their excellent guidance and immense encouragement throughout the course of this Master of Science (MSc) research;

All members in the Oil Sands Research Group at the University of Alberta, for their kind assistance; and

The financial support from the Natural Sciences and Engineering Research Council (NSERC) of Canada, Industrial Research Chair in Oil Sands Engineering and Canadian Mining Industry Research Organization (CAMIRO).

Table of Content

List of Tables

List of Figures

Nomenclature

a	aggregation rate, (m^3/s)
A	cross-sectional area, m^2
B_{Ag}	birth rate of drops, (s^{-1})
C	constant, (dimensionless)
D_{Br}	death rate of drops, (s^{-1})
$\vec{F}$	body force, (N)
f_g	noncondensable mass fraction, (dimensionless)
f_v	vapor mass fraction, (dimensionless)
g	gravitational acceleration, (m/s^2)
G_b	turbulent kinetic energy due to buoyancy, (m^2/s^2)
G_k	turbulent kinetic energy due to velocity gradient, (m^2/s^2)
G_V	rate of drop volume change, (m^3/s)
k	turbulent kinetic energy, (m^2/s^2)
n	bubble number density, ($\#/m^3$)
p	number of particles, (dimensionless)
P_v	vapor pressure, (Pa)
P	local pressure, (Pa)
P_{B}	bubble surface pressure, (Pa)
$\mathfrak{R}_{\mathrm{B}}$	bubble radius, (m)
R	net phase change rate, (kg/s)
R_c	rate of condensation, (kg/s)
R_e	rate of evaporation, (kg/s)
S_{ij}	Mean rate of strain tensor, (s^{-1})
S_k	user defined source term, (dimensionless)
S_ε	user defined source term, (dimensionless)

t time, (s)

u velocity, (m/s)

V droplet volume, (m^3)

x spatial coordinate, (m)

Y_M turbulent kinetic energy due to fluctuations of overall dissipation energy, (m^2/s^2)

Ca Cavitation number

Greek letters

α phase volume fraction, (dimensionless)

β probability, (dimensionless)

ε energy dissipation rate, ($m^2.s^{-3}$)

ρ density, ($kg \cdot m^{-3}$)

μ viscosity, (Pa·s)

μ_t turbulent viscosity, (Pa.s)

σ surface tension, ($N.m^{-1}$)

σ_k turbulent Prandtl number, (dimensionless)

σ_ε turbulent Prandtl number, (dimensionless)

Γ diffusion coefficient, ($m^2\,s^{-1}$)

Subscripts

k phase

m mixture

l liquid

dr drift

V vapour phase

i inlet

o outlet

Chapter 1: Introduction

1.1 Overview of fine particle flotation

In the mineral processing industry, flotation is a major separation technique used widely to concentrate desired minerals. In froth flotation, hydrophobic mineral particles are selectively attached to air bubbles and hence removed in the form of the froth layer after being lifted to the top of mineral pulp. However, due to their low mass and the resulting low inertial forces hydrophobic fine particles which are smaller than 20µm have lower collision efficiency with bubbles and fail to attach to rising bubbles. As a result, they escape the flotation process, and end up in the tailings stream, resulting in loss of valuable minerals. The conventional flotation system provides an appropriate working environment for particles of sizes 10-200 µm, but not for finer particles [Trahar et al., 1976]. This is a major challenge faced by mineral industries today. Several research efforts are made in this area of fine particle flotation. Numerous techniques have been developed, which aimed at increasing the particle- bubble attachment by either decreasing the air bubble size or increasing the particle size by aggregation [Miettinen et al., 2009]. Warren [Warren, 1975] reported that increasing the shear forces in the pulp increases the fine particle flotation and explained it due to the aggregation of fine particles in a high shear environment. Many researchers [Rubio, 1978], [Bulatovic et al., 1989] reported the improvement of fine particle flotation by high intensity conditioning of the feed stream and attributed this due to

the high flocculation of fines by shear. Later, Zhou and co-workers reported an increase in fine particle flotation when slurry is conditioned by passing through a cavitation tube prior to flotation [Zhou et al., 1994, 1995, 1997, 2009]. In their study, the improved flotation is attributed to the in-situ bubble formation by hydrodynamic cavitation on hydrophobic particles, which then helps the fine particle to aggregate. Wei and co-workers [Wei et al., 2005] conducted bubble size measurements using a high speed CCD technology in a high intensity agitated system and reported presence of cavitated bubbles. In their study the process of aggregate formation is assigned to the bridging action of fine bubbles which are produced in situ on the surface of fine particles by cavitation. Tao also reported increase in fine coal flotation when slurry passed through a cavitation tube [Tao et al., 2006]. They stated that the pico-bubbles generated by hydrodynamic cavitation nucleate at the surface of hydrophobic particles, which provide ultrafine particles adhere to pico-bubble without the need of collision. They also stated that particles are less likely to detach from smaller bubbles due to their lower acceleration force and centrifugal force associated with the detachment process reducing the probability of detachment.

1.2 Hydrodynamic cavitation

Hydrodynamic cavitation is the formation of vapor bubbles of a fluid by rupture of liquid in regions where the pressure falls below the vapor pressure. Cavitation is widely studied as a phenomenon which affects the performance of many types of equipment, such as pumps, inducers, propellers and injectors, and it is considered to be an undesirable part of fluid flow. Arndt [Arndt, 1981] investigated about its occurrence and impact on the performance of fluid machinery and hydraulic structures and emphasized about the mechanics of inception. Cavitated bubble implosions cause extreme effects locally, such as liquid jets of up to 1000 km/hr, pressure of up to 2000 atm and temperatures of up to 5000 ^{O}K**.** Cavitation phenomenon has been extensively studied to understand its role in erosion, noise and vibration in ship propellers. Cavitation

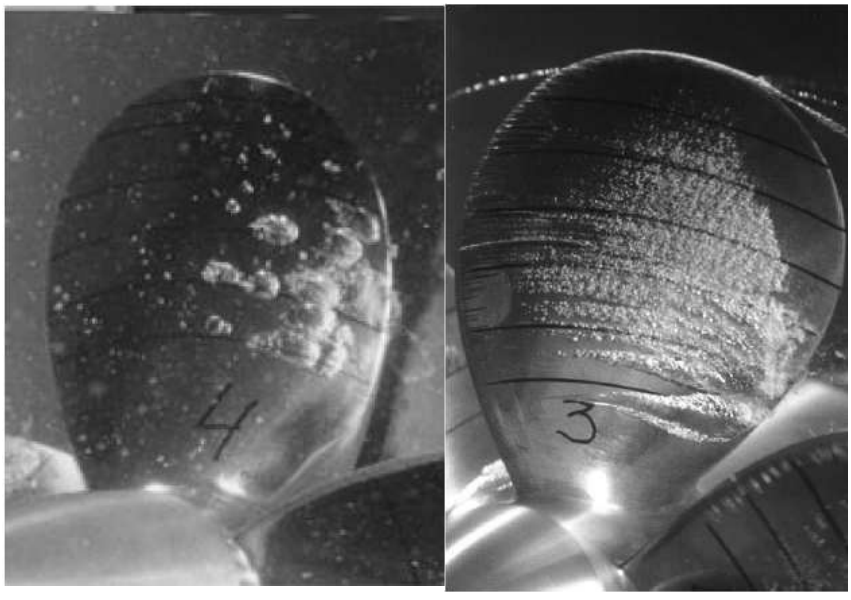

Figure 1-1: Bubble cavitation on a ship propeller at low nuclei content (left) and high nuclei content (right) [Kuiper, 1998]

phenomenon has been put in to a good use such as in ultrasonic cleaning devices and other liquid processes including mixing, blending, deagglomeration, wet-milling and micro-grinding of particles, and cell disintegration. Kuiper reported that the surface roughness of ship impellers, size and amount of the nuclei present (Figure 1-1), and flow Reynolds number, all affect the cavitation inception [Kuiper, 1998]. As shown in the Figure 1-2, tip vortex cavitation occurs along the tip of the impeller and sheet cavitation occurs on the blade.

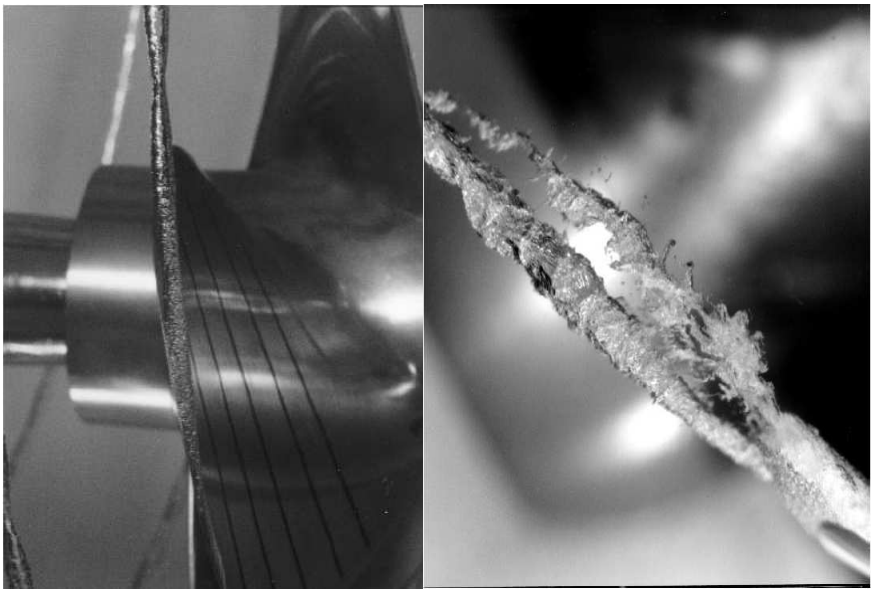

Figure 1-2: Shows the cavitated bubbles on the tip of a propeller blade (left) and the developed tip vortex cavitation. [Kuiper, 1998]

Nurick was the first to study about the cavitation phenomenon in an orifice flow [Nurick, 1976]. One of the main contributions of Nurick is to define the cavitation number (Ca) which takes account of all dynamic variables from the inlet manifold to the outlet.

$$Ca = \frac{Pi - Pv}{Pi - Po} \quad (1)$$

Where Pi is the inlet pressure and Po is the outlet pressure and Pv is the vapor pressure. Cavitation number is a parameter which has been used in the literature to characterize the potential for a flow to cavitate. Every flow has a cavitation number and when this value is very high flow is single phase. When cavitation number is reduced below a certain value, nucleation will first occur in a certain value of cavitation number which is called cavitation inception number Ca^*. Further reductions in cavitation number will increase the vapor formed. Cavitation includes initial formation of bubbles (inception) to large scale attached cavities (super-saturation). These cavities are usually nucleated at solid liquid interfaces, on sub-micron sized contaminant particles, uneven hydrophobic surfaces or micro-bubbles of noncondensable gases in the liquid. This type of cavitation is known as heterogeneous cavitation. In the case of homogeneous cavitation, weak points are created by thermal fluctuations (due to kinetic energy of the molecule) within the liquid, which form temporary microscopic voids that act as the nuclei for rupture and growth of cavities to macroscopic bubbles. Homogeneous cavitation is less practical in real systems due to the presence of various types of impurities. In fact the presence of hydrophobic surfaces would enable cavitation at a pressure well above the vapor pressure of the liquid [Brennen, 1995]. In flotation therefore, the hydrodynamically generated

cavities can be nucleated on the hydrophobic surface of particles and help lift them to the froth layer for separation. Zhou described the possible mechanism as shown in Figure 1-3 for fine particle aggregation and flotation by in situ bubble formation on hydrophobic surfaces by hydrodynamic cavitation [Zhou et al., 1997]. The two-stage attachment in which the cavitated tiny bubbles attach to a mineral particle first and then those tiny bubbles coalesce with flotation size bubbles is illustrated in Figure 1-3a.The bubble bridging mechanism, which increases the apparent particle size and thus increases the collision probability with flotation sized bubbles is shown in Figure 1-3b.

Hydrodynamic cavitation has been extensively studied computationally by many authors. There are mainly two models to calculate cavitating flows which are two-fluid model and mixture model. Of

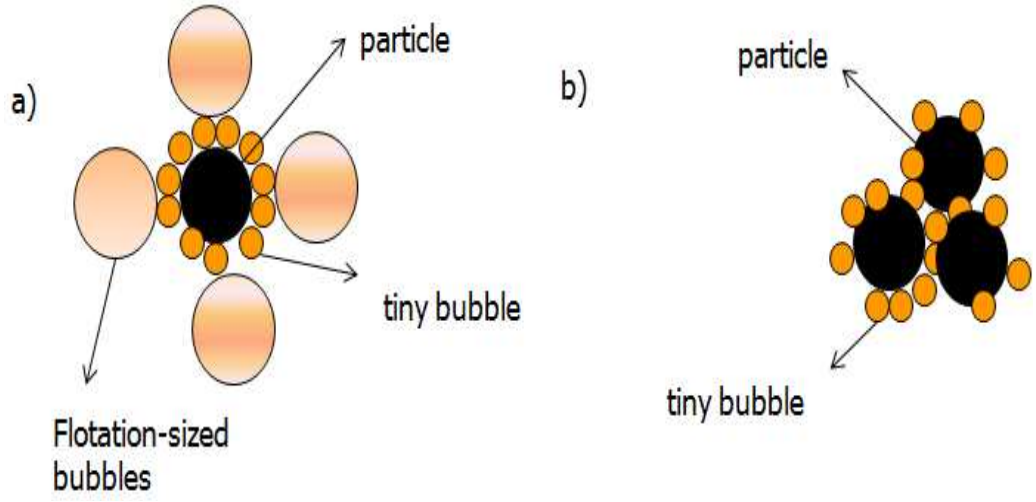

Figure 1-3: Schematic representation of possible mechanism for fine particle flotation by hydrodynamic cavitation: a) Two stage attachment; cavitated tiny bubbles attach to a mineral particle, which is then attach to a flotation-sized bubble by coalescence of the tiny bubble with the flotation size bubble b) enhanced coagulation by bubble bridging.

which mixture model is widely used for cavitating flows as it assumes mixture properties for the two phases for the entire computing domain. Thus the governing equation reduces to one set of continuity and momentum equation and a vapor fraction equation for the vapor phase. Singhal [Singhal et al., 2002] proposed a cavitation model in which cavitation mass transfer between liquid to vapor phase is formulated using Rayleigh-Plesset equation. They applied this model to pumps and inducers [Athavale et al., 2002] and the results showed cavitation zones on the leading-edge suction side of each of the machines as expected. Later, Susan-Resiga [Susan-Resiga et al., 2002] used the Singhal model to simulate the cavitating flow in Francis Turbine and calculated cavitation inception number. Again, Aschenbrenner used the same model to predict the unsteady turbulent flow and compared with experiments [Aschenbrenner et al., 2006]. Simulation code developed with Rayleigh-Plesset equation for cavitation simulation to numerically determine the regions of cavitation erosion on the blades of the mixed-flow pump impeller and centrifugal pump respectively was found to be in good agreement with experimental observations [Zima et al., 2004, Fukaya et al., 2008]. A mixture model with modified mass transfer expression for simulating cavitating flow around a 3D hydro foil was used by Liu [Liu et al., 2008]. The turbulence model used was RNG k-ϵ turbulence model and results agreed well with test data published in the literature. The Singhal cavitation model was used by Ding [Ding et al., 2009] to validate a three

dimensional CFD simulation tool, to predict the pump performance and cavitation for industrial applications.

1.3 Objective of the study

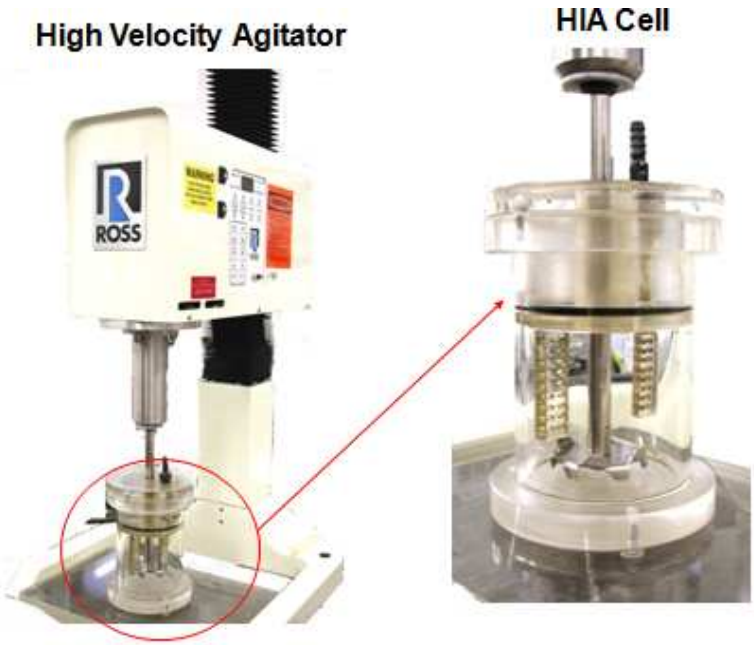

Figure 1-1: Experimental set up for a laboratory High Intensity Agitation Cell (HIA) cell

In this study we investigate the formation of hydrodynamic cavities using computational fluid dynamics (CFD) modeling in a high intensity conditioning system, i.e., in a cavitating tube and in a laboratory size high intensity agitation (HIA) cell (Figure 1-4). The HIA cell is a specially designed tank in which the impeller off-bottom clearance and the tank diameter to impeller diameter ratio are reduced to dissipate more turbulent

energy than in conventional flotation cell to enhance hydrodynamic cavitation. The CFD modeling has been used extensively to study flow patterns in conventional flotation cells. The predicted velocity was found in agreement with measured values [Koh et al., 2003, Song et al., 2009]. CFD study can provide a theoretical basis for impeller design by calculating the flow field characteristics such as local pressure and velocity distribution, location of cavity formation and to study the effect of different operating parameters on the flow field characteristics. This is invariably difficult to achieve from an experimental study on a flotation cell.

In a stirred tank, specifically near the impeller zone and baffles, a local increase in the velocity can lead to development of low pressure regions. If the pressure drops below the vapor pressure, vaporization of fluid can occur. Bubble dynamics is the foundation for understanding and predicting cavitation in an agitation system. The growth of a single vapor bubble in a liquid is governed by Rayleigh-Plesset equation. This equation, in combination with momentum and mass transport equations constitute the cavitation modeling. The volume fraction of the vapor phase can be calculated and used in conjunction with the population balance transport equation to predict drop size distributions of the dispersed vapor phase.

Chapter 2: Theory of Flow and Cavitation Model

The cavitation is modeled using ANSYS FLUENT's [ANSYS Fluent 12.0., 2009] cavitation model. This model solves the multiphase flow equations, with mass transfer due to cavitation as the source and sink terms in liquid and vapor continuity equations. The multiphase flow is calculated using the Mixture model, which treats the phases as interpenetrating continua [ANSYS Fluent 12.0]. The mixture model solves the momentum and continuity equation for the mixture and the volume fraction equation for the secondary phase. The turbulence is solved using the realizable k-ϵ model. The interphase mass transfer is solved using a modified form of Rayleigh-Plesset equation which is derived by Singhal [Singhal et al., 2001]

2.1 Flow model theory

2.1.1 Flow model

The continuity equation for the mixture is,

$$\frac{\partial(\rho_m)}{\partial t} + \nabla.(\rho_m \vec{u}_m) = 0 \qquad (2)$$

where $\vec{u}_m$ is the mass-averaged velocity given by

$$\vec{u}_m = \frac{\sum_{k=1}^{n} \alpha_k \rho_k \vec{u}_k}{\rho_m} \qquad (3)$$

ρ_m is the density of mixture given by

$$\rho_m = \sum_{k=1}^{n} \alpha_k \rho_k \qquad (4)$$

α_k is the volume fraction of phase k. and ρ_k is the density of phase k.

The momentum equation for the mixture can be obtained by summing the individual momentum equations for all phases [Batchelor, 1967], shown by

$$\frac{\partial}{\partial t}(\rho_m \vec{u}_m) + \nabla.(\rho_m \vec{u}_m \vec{u}_m) = -\nabla p + \nabla.\left[\mu_m\left(\nabla \vec{u}_m + \nabla \overrightarrow{u}^T_m\right)\right] + \rho_m \overrightarrow{g} + \overrightarrow{F} + \nabla.\left(\sum_{k=1}^{n} \alpha_k \rho_k \vec{u}_{\mathrm{dr,k}} \vec{u}_{\mathrm{dr,k}}\right) \quad (5)$$

where n is the number of phases, $\overrightarrow{F}$ is a body force, and μ_m is the viscosity of the mixture, given by

$$\mu_{\mathrm{m}} = \sum_{\mathrm{k=1}}^{\mathrm{n}} \alpha_{\mathrm{k}} \mu_{\mathrm{k}} \quad (6)$$

$\vec{u}_{\mathrm{dr,k}}$ is the drift velocity for secondary phase k, defined as

$$\overrightarrow{u}_{dr,k} = \overrightarrow{u}_k - \overrightarrow{u}_m \quad (7)$$

The term $\nabla.(\rho_m \vec{u}_m \vec{u}_m)$ represents the kinetic energy forces, $\frac{\partial}{\partial t}(\rho_m \vec{u}_m)$ represents inertial forces and $\left[\mu_m\left(\nabla \vec{u}_m + \nabla \overrightarrow{u}^T_m\right)\right]$ represents viscous forces.

The volume fraction equation for the secondary phase is obtained from the continuity equation of that phase as given by

$$\frac{\partial}{\partial t}(\alpha_p \rho_p) + \nabla.(\alpha_p \rho_p \vec{u}_m) = \nabla.(\alpha_p \rho_p \vec{u}_{\mathrm{dr},p}) + \sum_{q=1}^{n}(\dot{m_{qp}} - \dot{m_{pq}}) \quad (8)$$

2.1.2 Turbulence model

The turbulence in a given system is taken into account by solving equation for k (turbulent kinetic energy) and ϵ (turbulent dissipation rate) as per the realizable k-ϵ model in ANSYS Fluent 12.0, as given by

$$\frac{\partial}{\partial t}(\rho k) + \frac{\partial}{\partial x_j}(\rho k u_j) = \frac{\partial}{\partial x_j}\left[\left(\mu + \frac{\mu_t}{\sigma_k}\right)\frac{\partial k}{\partial x_j}\right] + G_k + G_b - \rho\epsilon - Y_M + S_k \tag{9}$$

and

$$\frac{\partial}{\partial t}(\rho\epsilon) + \frac{\partial}{\partial x_j}(\rho\epsilon u_j) = \frac{\partial}{\partial x_j}\left[\left(\mu + \frac{\mu_t}{\sigma_\epsilon}\right)\frac{\partial \epsilon}{\partial x_j}\right] + \rho C_1 S_\epsilon - \rho C_2 \frac{\epsilon^2}{k + \sqrt{\upsilon\epsilon}} + C_{1\epsilon}\frac{\epsilon}{k} C_{3\epsilon} G_b + S_\epsilon \tag{10}$$

where

$$C_1 = \max[0.43, \frac{\eta}{\eta + 5}], \quad \eta = S\frac{k}{\epsilon}, \qquad and\ S = \sqrt{2S_{ij}S_{ij}} \tag{11}$$

In equation 10, G_k, G_b and Y_M are the turbulent kinetic energy due to mean velocity gradient, buoyancy, and fluctuations due to overall dissipation energy, respectively; S_K and S_ϵ are the user defined source terms; σ_k and σ_ϵ are turbulent Prandtl numbers; and C_1 and C_2 are constants; S_{ij} is the mean rate of strain tensor.

Turbulent viscosity is obtained as;

$$\mu_t = \rho C_\mu \frac{k^2}{\epsilon} \qquad (12)$$

where C_μ is a function of the mean strain and rotation rates, the angular velocity of the system rotation, and the turbulence fields.

2.2 Cavitation model theory

In cavitation, the mass transfer of vapor (evaporation and condensation) is calculated by the following vapor transport equation:

$$\frac{\partial}{\partial t}(\alpha\rho_v) + \nabla.(\alpha\rho_v\vec{u}_v) = R_e - R_c \qquad (13)$$

where υ is the vapor phase, α is the vapor volume fraction, and ρ_v is the density of vapor. R_e and R_c in equation 13 are the vapor generation and condensation rate terms, which account for the mass transfer between phases.

The bubble growth and collapse are governed by the bubble dynamics equation which is given by the Rayleigh-Plesset equation [Brennen, 1995] as;

$$\mathfrak{R}_B \frac{d^2\mathfrak{R}_B}{dt^2} + \frac{3}{2}\left(\frac{d\mathfrak{R}_B}{dt}\right)^2 = \left(\frac{P_B - P}{\rho_l}\right) - \frac{4u_l}{\mathfrak{R}_B}\mathfrak{R}_B - \frac{2\sigma}{\rho_l\mathfrak{R}_B} \qquad (14)$$

where $\mathfrak{R}_B$ is the bubble radius, ρ_l is the liquid density, P_B is the bubble surface pressure, P is the local pressure, and σ is the surface tension.

Neglecting the second order terms and the surface tension term equation 14 reduces to

$$\frac{d\Re_B}{dt} = \sqrt{\frac{2}{3}\frac{P_B - P}{\rho_l}} \tag{15}$$

Equation for net phase change rate was derived by Singhal [Singhal et al., 2001] as follows;

Liquid phase continuity equation:

$$\frac{\partial}{\partial t}[(1-\alpha)\rho_l] + \nabla.\left[(1-\alpha)\rho_l \vec{u}\right] = -R \tag{16}$$

Vapor phase continuity equation:

$$\frac{\partial}{\partial t}(\alpha\rho_v) + \nabla.\left(\alpha\rho_v \vec{u}\right) = R \tag{17}$$

Mixture continuity equation:

$$\frac{\partial(\rho)}{\partial t} + \nabla.(\rho \vec{u}) = 0 \tag{18}$$

where mixture density ρ is defined as:

$$\rho = \alpha\rho_v + (1-\alpha)\rho_l \tag{19}$$

Combining equations 17, 18 and 19, a relationship between mixture density and vapor volume fraction is obtained as:

$$\frac{d\rho}{dt} = -(\rho_l - \rho_v)\frac{d\alpha}{dt} \tag{20}$$

Assuming that the bubble to be of spherical shape, vapor volume fraction α is then related to bubble number density n and bubble radius, $\Re_B$ as:

$$\alpha = n \times (\frac{4}{3}\pi \, \Re_B{}^3) \tag{21}$$

Combining the above two equations (20 and 21) gives

$$\frac{d\rho}{dt} = -(\rho_l - \rho_v)(n4\pi)^{\frac{1}{3}} (3\alpha)^{\frac{2}{3}} \frac{d\Re_B}{dt} \tag{22}$$

Using equation 15, and combining equations 16, 17, 20 and 22 give an expression for net phase change rate R as

$$R = (n4\pi)^{\frac{1}{3}} (3\alpha)^{\frac{2}{3}} \frac{\rho_v \rho_l}{\rho} \sqrt{\frac{2}{3}\frac{P_v - P}{\rho_l}} \tag{23}$$

Equation 23 expression gives the rate of vapor generation by evaporation and condensation. This equation can be written in terms of $\Re_B$ as

$$R = \frac{3\alpha}{\Re_B} \frac{\rho_v \rho_l}{\rho} \sqrt{\frac{2}{3}\frac{P_v - P}{\rho_l}} \tag{24}$$

Equation 24 indicates that the unit volume mass transfer depends on vapor density, liquid density and the mixture density. Here P, local pressure is the cell centre pressure and P_B is equal to vapor pressure P_v i.e

$$P_B = P_v \tag{25}$$

Again, the proposed model for vapor transport given as follows [Zwart, 2005] :

$$\frac{\partial}{\partial t}(f_v \rho) + \nabla \cdot (f_v \rho \vec{u}_v) = \nabla \cdot (\Gamma \nabla f_g) + R_e - \mathrm{R_c} \tag{26}$$

where f_v is vapor mass fraction, f_g is noncondensable mass fraction and Γ is the diffusion coefficient. R_e and R_c in equation 26 are evaporation and condensation rate terms which are defined as:

(when $\mathrm{P_v} \geq \mathrm{P}$) $\mathrm{R_c} = 0$ and

$$R_e = F_{vap} \frac{max(1.0,\sqrt{k})(1-f_v-f_g)}{\sigma} \rho_v \rho_l \sqrt{\frac{2}{3}\frac{P_v-P}{\rho_l}} \qquad (27)$$

when $\mathrm{P}_v \geq \mathrm{P}$. Otherwise $\mathrm{R_e}=0$ and

$$\mathrm{R_c} = \mathrm{F_{cond}} \frac{\max(1.0,\sqrt{k})(1-\mathrm{f_v}-\mathrm{f_g})}{\sigma} \rho_\mathrm{v} \rho_\mathrm{l} \sqrt{\frac{2}{3}\frac{\mathrm{P}-\mathrm{P_v}}{\rho_\mathrm{l}}} \qquad (28)$$

when $\mathrm{P}_v < \mathrm{P}$. The constants in equation 27 and 28 are $\mathrm{F_{vap}}$=0.02 and $\mathrm{F_{cond}}$=0.01. The saturation pressure is corrected to accommodate the changes due to turbulent pressure fluctuations by;

$$P_v = P_{sat} + \frac{1}{2}(0.39k) \qquad (29)$$

where k is turbulent kinetic energy. These mass transfer rate terms are a function of the flow parameters such as local pressure, fluid velocity and turbulence, and fluid physical properties such as liquid and vapor phase densities, saturation pressure and vapor liquid surface tension [Singhal et al., 2001]

2.3 Population balance theory

Population balance model (PBM) in the ANSYS Fluent 12.0 is used to obtain the bubble size distribution of the cavitated bubbles in orifice

flow. It was found to be too complicated to apply PBM to a 3D model as in HIA cell system. For this reason, the size distribution studies were conducted only for the orifice flow system. This modeling concept uses a number density function, $n(r,V,t)$ to account for population of bubbles of volume V per unit volume. The local average number density (number of bubbles per unit volume) can be given by

$$N(r,t) = \int_{\Omega_V} n(r,V,t)dV \tag{30}$$

The volume fraction of all drops is given by:

$$\alpha(r,t) = \int_{\Omega_V} n(r,V,t)VdV \tag{31}$$

For a population of bubbles having volume V, the steady-state transport equation for the number density function or population balance equation (PBE) can be written as

$$\frac{d}{dt}[n(r,V,t)] = B_{Ag} - D_{Ag} + B_{Br} + D_{Br} \tag{32}$$

where B_{Ag} is the birth rate of bubbles through aggregation, D_{Br} is the death rate of bubbles through breakage, D_{Ag} is the death rate by aggregation and B_{Br} is the birth rate by breakage.

The boundary conditions are given by:

$$n(V,t=0) = n_V \; ; \; n(V=0,t)G_V = n_0 \tag{33}$$

where n_V and n_0 are the initial number density function. The substantial derivative of the number density function becomes

$$\frac{d}{dt}[n(r,V,t)] = \frac{\partial}{\partial t}[n(r,V,t)] + \nabla \cdot [\vec{u}n(r,V,t)] + \frac{\partial}{\partial V}[G_V n(r,V,t)] \quad (34)$$

where $\vec{u}$ is the bulk fluid velocity and G_V is the rate of bubble volume changes with time.

2.3.1 Aggregation

When two droplets of volume $V - V'$ and V' collide to form a droplet of volume V, it results in aggregation. The particle birth rate through aggregation is expressed as

$$B_{Ag} = \frac{1}{2}\int_0^V a(V - V', V')\, n(V - V', t) n(V') dV' \quad (35)$$

The aggregation rate, $a(V - V', V')$ [m^3/s], the rate of volume aggregation due to collision between bubbles of volume $V - V'$ and V' to form a bubble of volume V is often expressed as the product of:

- The frequency of collision between particles of volume $V - V'$ and V'
- The efficiency of aggregation between particles of volume $V - V'$ and V'

A factor of one half is included so as not to count each collision event twice.

The particle death rate through aggregation is expressed as

$$D_{Ag} = \int_0^\infty a(V, V')\, n(V, t) n(V', t) dV' \quad (36)$$

In this case, limits from 0 to infinity is used, since death by aggregation does not give birth to a bubble of volume V.

The aggregation rate function can be modeled through ANSYS Fluent 12.0 by a constant or through the Luo model, the free molecular model, the turbulent model and any user-defined model.

2.3.2 Breakage

Breakage occurs as a result of shear or other forces applied to individual droplets. These forces are the result of the nature of the flow field surrounding a droplet. The birth rate due to breakage can be given as

$$B_{Br} = \int_{\Omega_V} p g(V') \beta(V|V') n(V', t) dV' \qquad (37)$$

where p is the number of particles generated by a breakage event, and the breakage rate $g(V')$ is the rate of drop breakage of volume V' per unit time (m^3/s). The probability density function (PDF), $\beta(V|V')$ gives the probability of particles breaking from volume $V'$to a particle of volume V (m^3/s).

The death rate due to breakage is given as

$$D_{Br} = g(V) n(V, t) \qquad (38)$$

A more detailed description of the population balance equation and its applications are given by ANSYS Fluent 12.0., 2009.

Chapter 3: Computational Frame Work

3.1 Geometry of HIA cell

The geometry of the tank and the impeller used for the simulation is the same as that of a laboratory HIA cell. The tank diameter is 7.65 cm and it has two baffles. It is filled with water to a level of H= 7.60 cm. The impeller is a 2-vane flat blade with a diameter of 5.75 cm. All the dimensions used are shown in Figure 3-1. The geometry of the mesh is generated using the CFD software, GAMBIT and it is shown in Figure 3-2. The mesh used is tetrahedral in shape. Finer mesh is used at the impeller region to capture the sub-micron size bubbles.

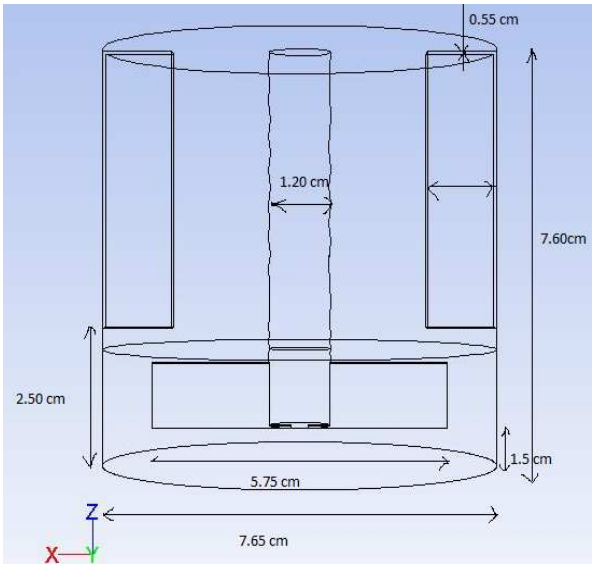

Vessel diameter, D_T	7.65 cm
Vessel height, H	7.60 cm
Baffle width, J	1.34 cm
Baffle thickness	0.55 cm
Number of baffles	2
Impeller diameter, D	5.75 cm
Bottom clearance, E	1.5 cm
D/D_T	0.7529
J/D_T	0.175
C/D_T	0.196

Figure 3-1: Dimensions of the HIA cell used for simulation

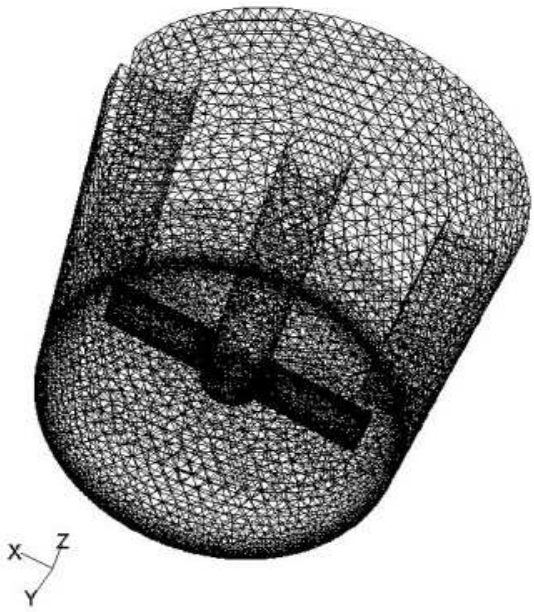

Figure 3-2: Mesh for HIA cell

Four types of impellers (flat blade 2-vane (no. of cells=170235), flat blade 4-vane (no. of cells=234683), pitched blade 4 vane (no. of cells=232594) and radial disc turbine 6-vane (no. of cells=266874)) are used for simulation to study the flow pattern and other flow properties in a HIA cell at constant RPM of 2000. Figure 3-3 shows the types of impellers used.

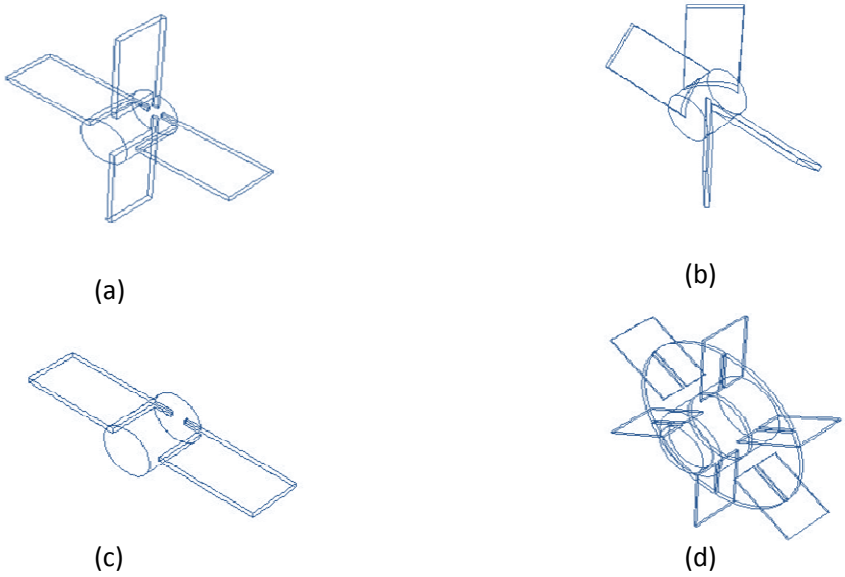

Figure 3-3: Four types of impellers studied: a) straight 4-vane, b) pitched 4-vane, c) straight 2-vane, and d) radial disc 6-vane

The geometry of different impellers used for simulation has the same diameter of 5.75 cm with all other tank dimensions remaining the same. The working fluid used was water, with a density of 998.2 kg/m^3 and a viscosity of 0.001 Pa-s at a room temperature of 20^{o}C.

3.2 Simulation parameters

The moving parts are computationally immobilized using a multiple reference frame (MRF) equation, in which individual zones are assigned with different RPM. The flow field is calculated using a steady state assumption and a realizable turbulence model, which is the most suitable for rotating flows. Boundary conditions are set as RPM in the impeller

zone. The solution residuals are set to a value of 1x 10^{-05}. The results obtained are interpreted for flow patterns in the HIA cell.

Cavitation studies are done only with one type of impeller which is the 2-vane flat blade. The multiphase model used is the mixture model. The working fluid is considered as a two phase mixture of water and vapor (water at 20^{o}C as the primary phase and water vapor (density- 0.5542 kg/m^{3}, viscosity- 1.34 x 10^{-05} Pa s) as the secondary phase). In this model it treats phases as interpenetrating continua. The cavitation model used is the Singhal model with the following parameters; saturated pressure of 2367.8 Pa, a dissolved air content of 15 ppm, water liquid surface tension of 0.0717 N/m. Cavitation is studied at different impeller speed, dissolved air content and different water temperature.

3.3 Modeling of flow through a constriction

The cavitation simulation studies are exclusively conducted in a flow through constriction scenario to understand the behavior of cavitation in a turbulent flowing liquid.

The geometrical dimensions and the grid generated are shown in Figure 3-4. A steady state two dimensional axisymmetrical model is used for simulation. This two-dimensional computation is less time consuming and provides more accurate results than simulation in a three-dimensional geometry. Boundary conditions are set at pressure inlet and pressure outlet to vary the velocity in the system.

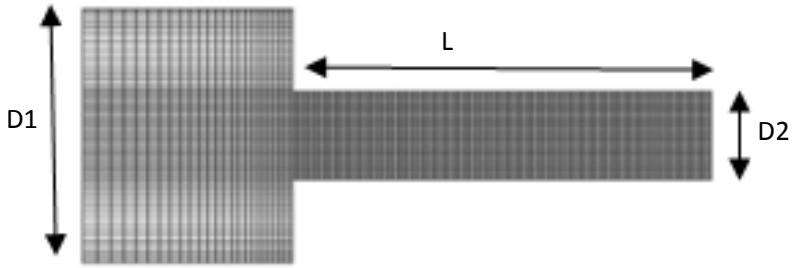

D1	1.15 cm
D2	0.4 cm
L/D2	8

Figure 3-4: Mesh for orifice flow simulation

The bubble size distributions of the cavitated bubbles in orifice are obtained using population balance. Implementation of the population balance model to an HIA cell is quite complicated as it required a finer mesh and computationally intensive. As it is, the cavitation module will not work if population balance module is enabled. The population balance model uses different methods of inbuilt mass transfer models to calculate phase changes, but cavitation mass transfer is not one of them. Hence a user defined function (UDF) (Appendix A) is used to incorporate mass transfer due to cavitation (equation 27) to Population Balanced model. The UDF calculates the nucleation rate term from the evaporation rate term (equation 27) as per relation below:

$$Nucleation\ Rate = \frac{Evaporation\ Rate}{\rho_{Vapor} * V_0} \qquad (39)$$

where V_0 is the volume of nucleated bubble. In this study we assume that the bubbles are nucleated with nucleation radius of 1 micron. ANSYS Fluent has an added constraint n_0, the nucleation rate, which be limited to 1x 10^{20} bubbles/sec.

Population balance simulations are conducted using discrete methods of solution, which gives the particle size distribution directly. This method requires specifying the range of particle sizes with span not more than two or three orders of magnitude. The bubble breakage frequency and aggregation frequency are calculated using the Luo model in ANSYS Fluent 12.0. UDF with a nucleation radius of 1 micron is simulated using discrete method.

3.4 Validation of simulation procedures

The flow of liquid in a laboratory HIA cell is approximated as a steady state system as it operates at constant RPM under the same conditions. As such fluid properties can change from point to point in the system but at any fixed point they remain constant. Moreover, authors like Song [Song et al., 2009] solved for a steady flow in a large scale flotation cell and obtained results for gas hold up which are in very good agreement with the experimental results. At an impeller speed of 1500 RPM and above, bubbles were observed in laboratory test and the same impeller speed is set as the boundary condition for impeller zone. The solution residuals for all the iterations are set to a value of 1x10^{-5}, in order to make

sure all the simulations are converged to same extent of solution. Multiple Reference Frame Model (MRF) is used to calculate the relative motion of moving impeller zone and the stationary walls. Athavale and his co-workers [Athavale et al., 2002] used k-ϵ turbulence model in their studies and obtained very good results with respect to cavitated vapor fraction. Various k-ϵ turbulence models like RNG, Standard and Realizable are tested to obtain turbulent dissipation rate in it and the volume average of turbulent dissipation rate in impeller zone is given in Table 3-1.

Table 3-1: Turbulence dissipation rate at impeller zone of a two-vane HIA cell at impeller speed of 200RPM

Turbulence Model	ϵ, m^2/s^3
Realizable	93.126
Standard	83.17317
RNG	8.6941

Realizable k-ϵ turbulence model showed the maximum average turbulent dissipation rate among the other models. The same model was used in this study to calculate turbulence. Nevertheless standard k-ϵ turbulence model predicted more intensive turbulent dissipation rate than the rest. Finer mesh is used at the impeller region to capture the sub-micron size bubbles.

Chapter 4: Results and Discussion

4.1 Impeller characterization

To begin with, the results of simulation at 2000 RPM for different impellers are interpreted to understand the flow patterns in the HIA agitation system. Obviously, it would be different from a standard agitation cell because of the geometric factors such as lower bottom clearance and lower impeller to tank diameter ratio in a HIA cell.

4.1.1 Flat 2-vane HIA cell

Figure 4-1 shows the velocity vector colored by velocity magnitude in a 2-vane HIA cell. The velocity at the tip of the impellers is the maximum of 7.56 m/s. The flow pattern shows a radial flow in the impeller zone with axial mixing at the bulk zone.

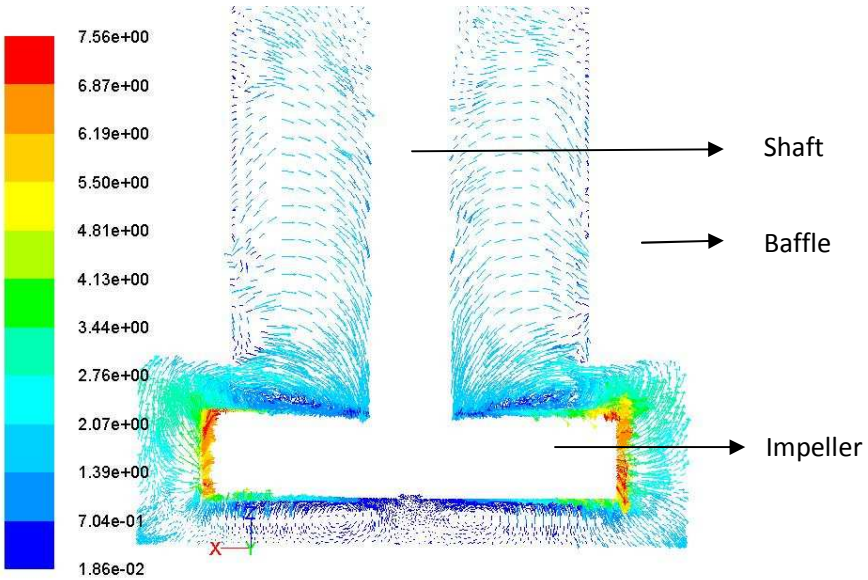

Figure 4-1: Velocity vector along a vertical cross section through impellers in a flat blade 2-vane HIA cell at 2000 RPM

At the bottom of impeller there is not enough mixing and predicted the lowest velocity of 1.86 m/s. Figure 4-2 also shows vortex formation in the impeller zone and an axial mixing pattern in a 2-vane HIA cell.

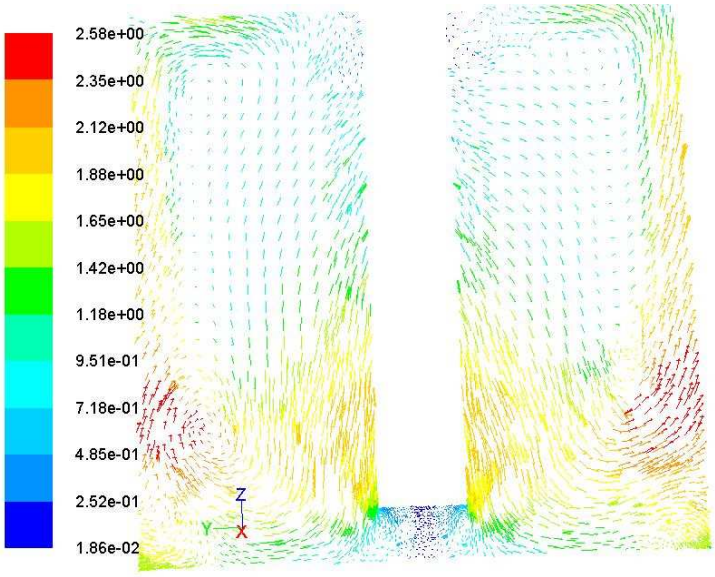

Figure 4-2: Velocity vector at a vertical cross sectional view along the tank where no baffles are present shows vortex formation at the impeller zone and an axial mixing pattern in a 2-vane HIA cell

The static pressure contours (Figure 4-3) predicted negative pressures at the vicinity of the impeller (-24100 Pa) and a pressure well below the vapor pressure of 2367 Pa throughout the impeller zone and some parts of bulk zone near the baffles.

The horizontal cross sectional view of static pressure contour (Figure 4-4) predicted a low pressure region behind the impellers (the flow is clockwise). The static pressure predicted is negative in those regions. This clearly shows that these regions can be potential cavitation inception sites.

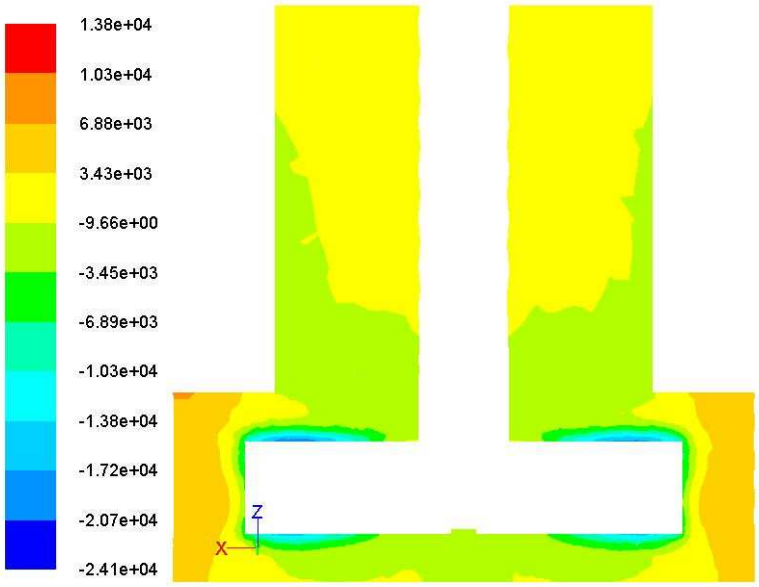

Figure 4-3: Pressure contour at vertical cross section of 2-vane HIA cell

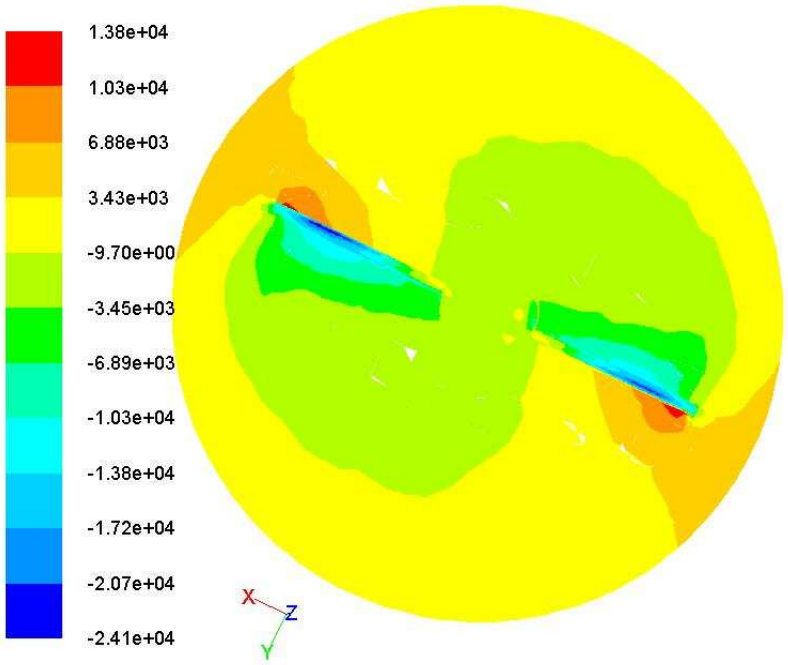

Figure 4-4: Horizontal cross sectional pressure contour showing low pressure zones behind the impellers in a 2-vane HIA cell

The turbulent kinetic energy contour of 2-vane HIA cell is shown in Figures 4-5 and 4-6. These contours indicate high intensity turbulent vortex formation behind the impellers where velocity is maximum and pressure is minimum. The other impellers studied also predicted a similar trend, even though flow patterns were different.

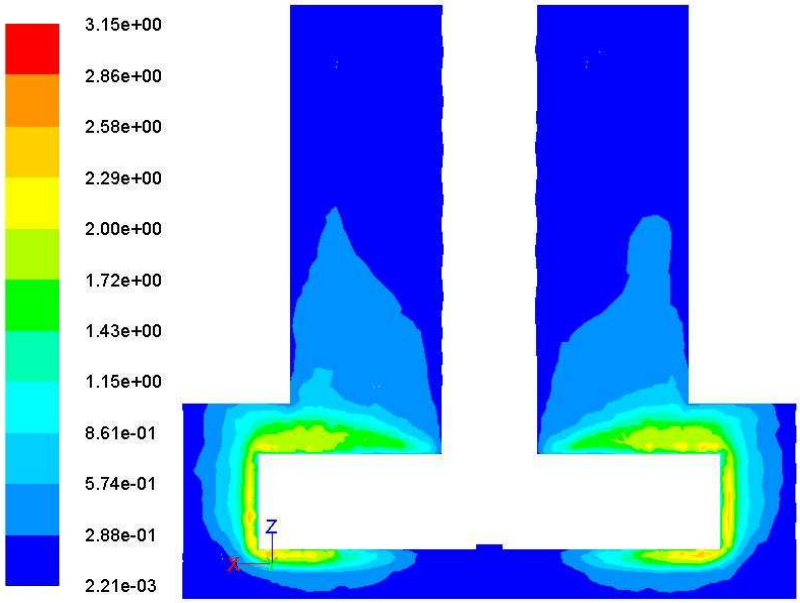

Figure 4-5: Contours of turbulent kinetic energy of 2-vane HIA cell, showing high turbulence at the impeller tip

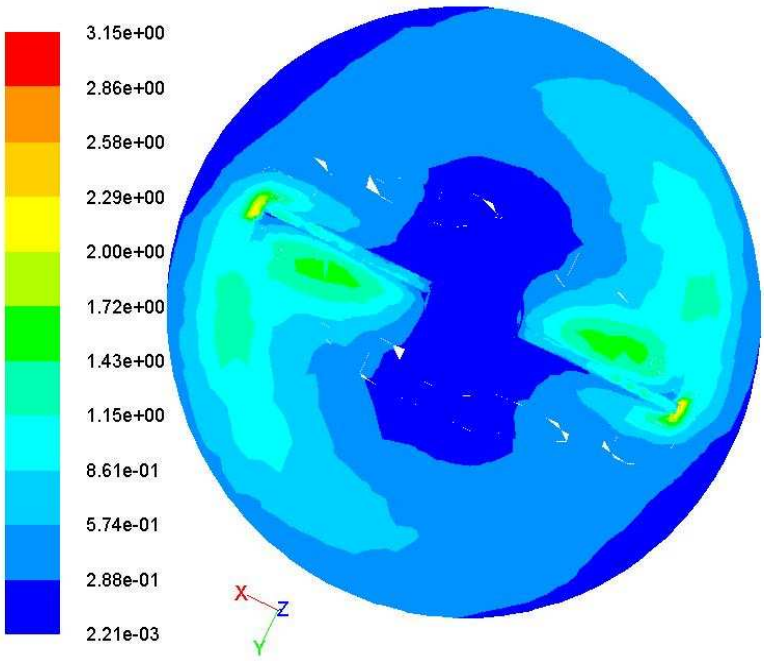

Figure 4-6: Contours of turbulent kinetic energy at a horizontal cross section, showing high turbulent vortex formation behind the impellers for 2-vane HIA cell

4.1.2 Pitched 4-vane blade impeller HIA cell

The velocity vector for a pitched blade (Figure 4-7) indicates a good axial mixing pattern with a more uniform velocity in the bulk and impeller zone. The results clearly indicate the well mixed zone below the impeller and hence good homogeneous mixing pattern of a down pumping pitched blade turbine.

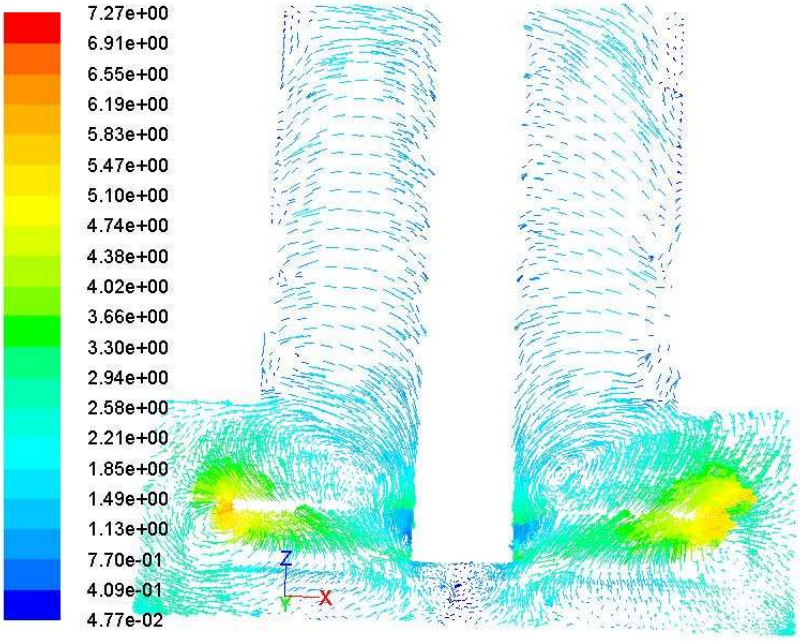

Figure 4-7: Velocity vector produced by pitched impellers showing a very good axial mixing pattern

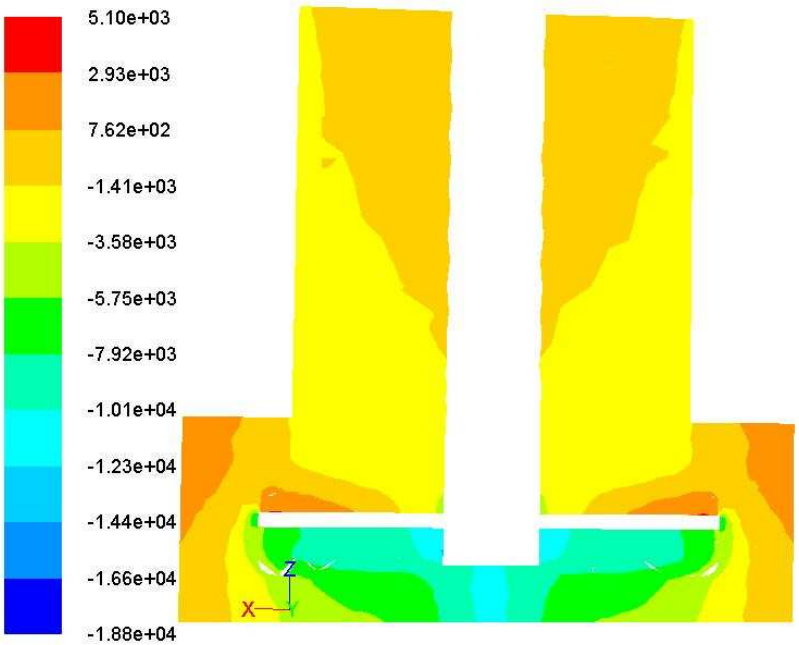

Figure 4-8: Static pressure contour for a pitched blade impeller HIA cell, showing a slightly lower negative pressure than in a flat blade 2-vane cells

The static pressure contour plot for a pitched blade HIA cell (Figure 4-8) showed a pressure distribution with slightly lower negative pressure than in the 2-vane flat blade cell. Here the minimum static pressure predicted is -18800 Pa. The turbulent kinetic energy distribution (Figure 4-9) showed less intensity in pitched blade impeller than in a 2-vane impeller. Here the maximum turbulent kinetic energy predicted is 2.18m^2/s^2 whereas for a 2-vane flat blade cell, it is 3.15m^2/s^2. This means that even though pitched blade gives a better mixing it has lesser turbulence and hence lower velocity and lower negative static pressure than a 2-vane flat blade cell.

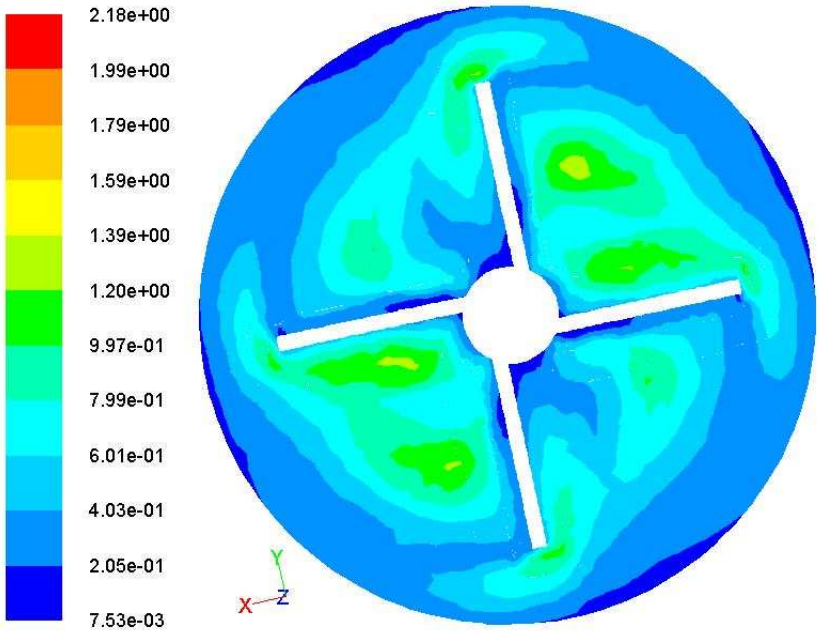

Figure 4-9: Contours of turbulent kinetic energy in a pitched 4-vane blade cell, showing lesser turbulence than in a 2-vane cell

4.1.3 Radial disc 6-vane HIA cell

The velocity vector and contour plots of flow parameters in a radial disc 6-vane cell is shown in Figures 4-10, 4-11 and 4-12. The flow pattern clearly indicates a radial mixing at impeller and an upward axial flow above and a downward axial flow below. This impeller produced the maximum velocity of 7.81 m/s and a more uniform mixing than the rest of the impellers. But it showed less turbulence and slightly lower negative static pressure than the 2-vane and 4-vane flat blade systems. These results indicate that radial disc 6-vane turbine in HIA cell imparts high velocity to the fluid with less turbulence and dissipation.

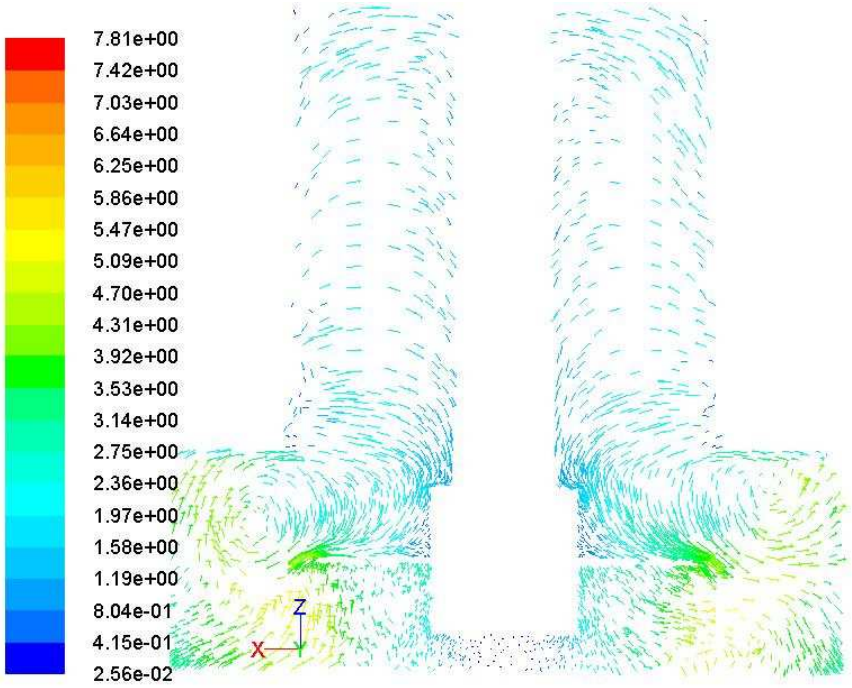

Figure 4-10: Velocity vector in a radial disc 6-vane cell showing upward axial mixing above impeller and a downward axial mixing below the impeller

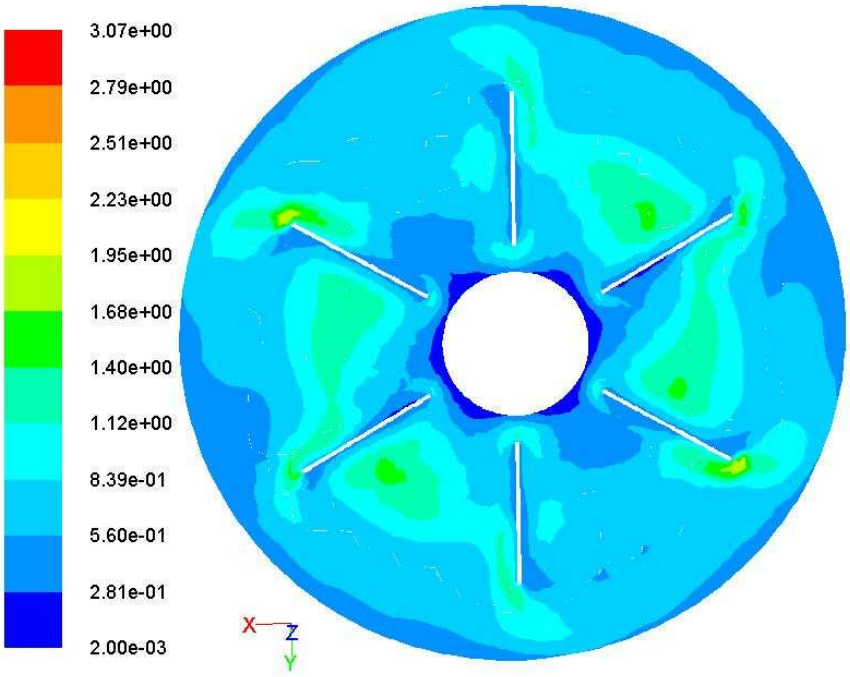

Figure 4-11: Contours of turbulent kinetic energy in radial disc 6-vane cell

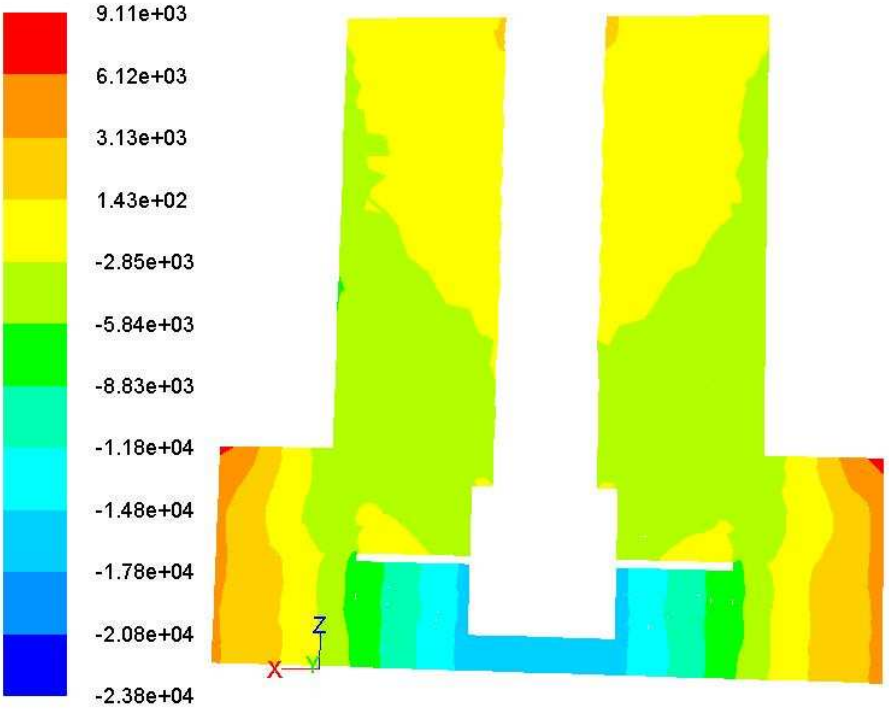

Figure 4-12: Contours of static pressure in a radial disc 6-vane cell

4.1.4 Flat 4-vane Impeller HIA cell

The flow parameter contours in a 4-vane cell is shown in Figures 4-13, 4-15 and 4-15. The velocity vector indicates that the flow is radial at the impeller zone. This type of impeller imparts an axial mixing, but it is not as effective as in a pitched 4-vane cell or in a radial disc cell. But this turbine dissipates maximum turbulence than any other types of turbines in an HIA cell.

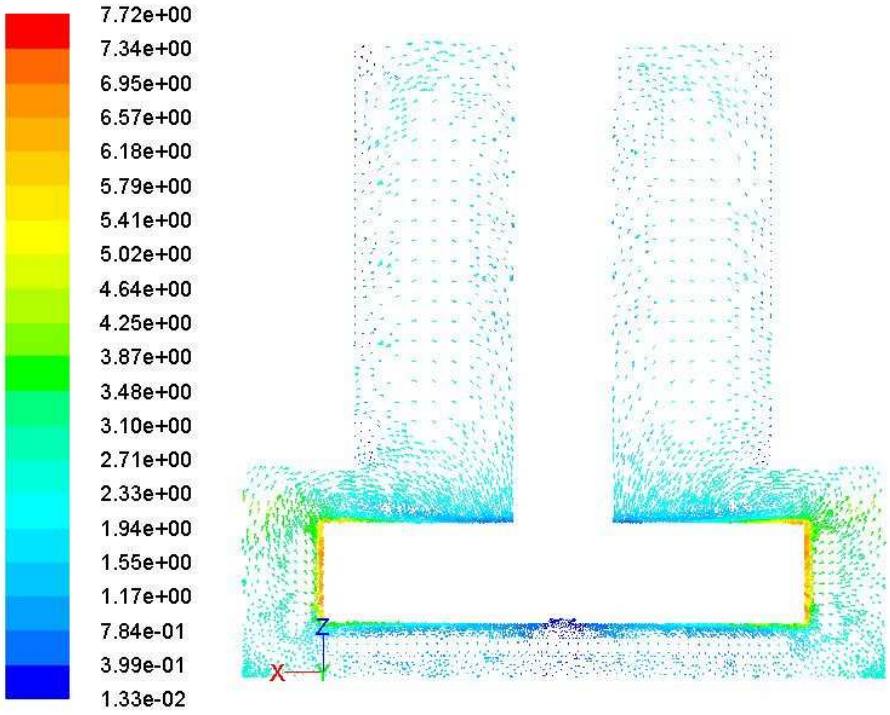

Figure 4-13: Velocity vectors colored by velocity magnitude in 4-vane cell

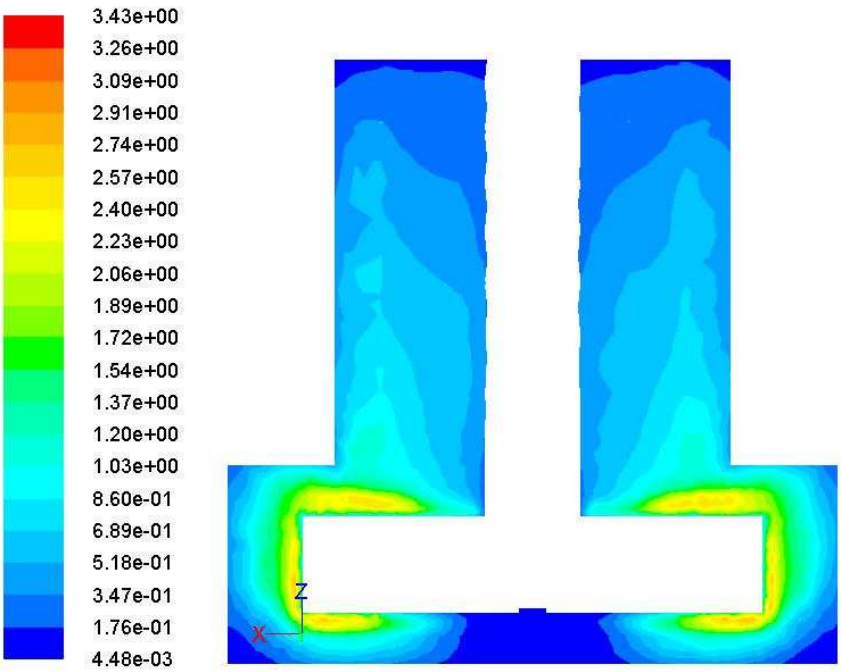

Figure 4-14: Contours of kinetic energy in a flat 4-vane impeller HIA cell

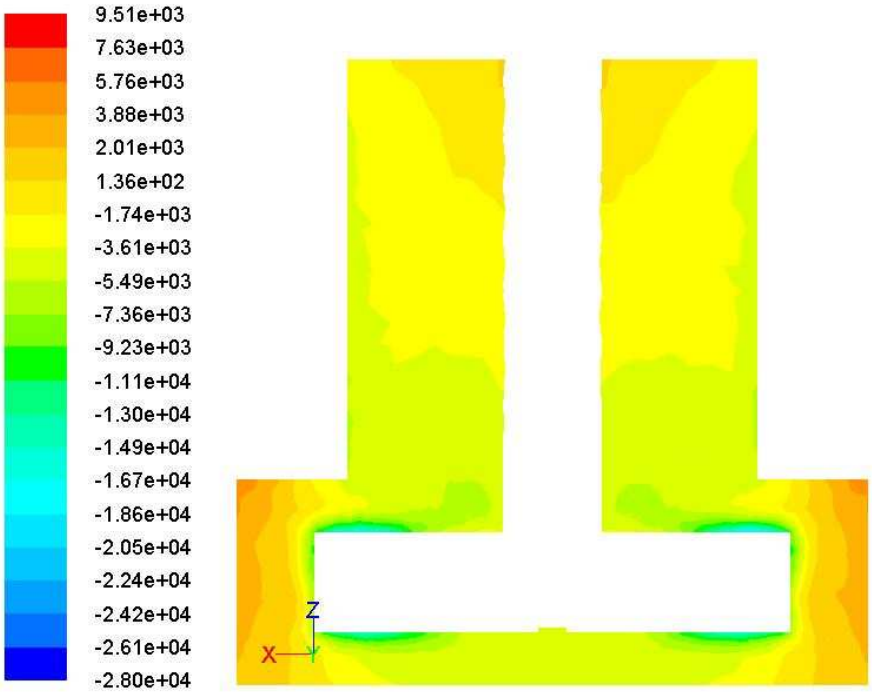

Figure 4-15: Contours of static pressure in a flat 4-vane impeller HIA cell

A comparison on all types of impellers studied here (Table 4-1) indicates that 4-vane turbine has the most potential to produce cavitation in the cell, as it creates the lowest pressure and highest turbulence in the system.

Table 4-1: Results predicted for impeller characterization study

Impeller type	Turbulent kinetic energy, m^2/s^2	Minimum static pressure, Pa	maximum velocity, m/s
Flat blade 2-vane	3.18	-24100	7.56
Pitched blade 4-vane	2.18	-18800	7.27
Flat blade 4- vane	3.43	-28000	7.72
Radial disc 6- vane	3.07	-23800	7.81

4.2 Hydrodynamic cavitation

4.2.1 Hydrodynamic cavitation in a flow through constriction

Firstly, the simulation is carried out for cavitation in an orifice flow. In this case no slip between bubbles and liquid is assumed. The material properties of water and vapor used are those at 27^oC. The parameters used for water are: density – 1000 kg/m^3, viscosity – 0.001 kg/ms, and vapor pressure – 3540 Pa, while for water vapor they are: density – 0.02558 kg/m^3, and viscosity – 1.26E-06 kg/ms. A constant value of 15 ppm of noncondensable gas mass fraction in the water is used for cavitation calculations. For air dissolved in water, 15 ppm is a typical value

at normal temperature and pressure. Inlet and outlet pressures of 5 and 0.95 atm are set as boundary conditions.

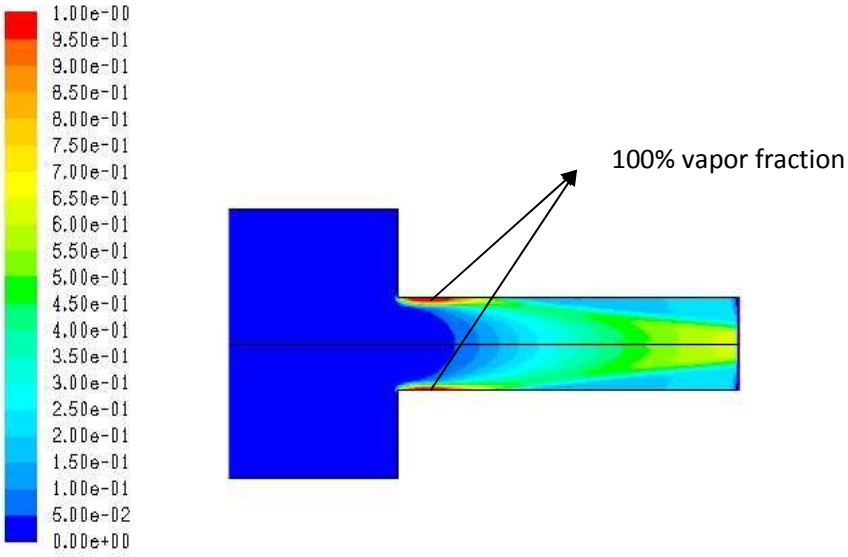

Figure 4-16: Contours of volume fraction in an orifice flow constriction

The contours of vapor volume fraction for an orifice flow constriction are obtained as shown in Figure 4-16. A strong cavitation of 100% near flow separation is found. The contour plots of static pressure (Figure 4-17) and velocity (Figure 4-18) predicted a minimum pressure of 3540 Pa and a velocity of 27 m/s at the throat area.

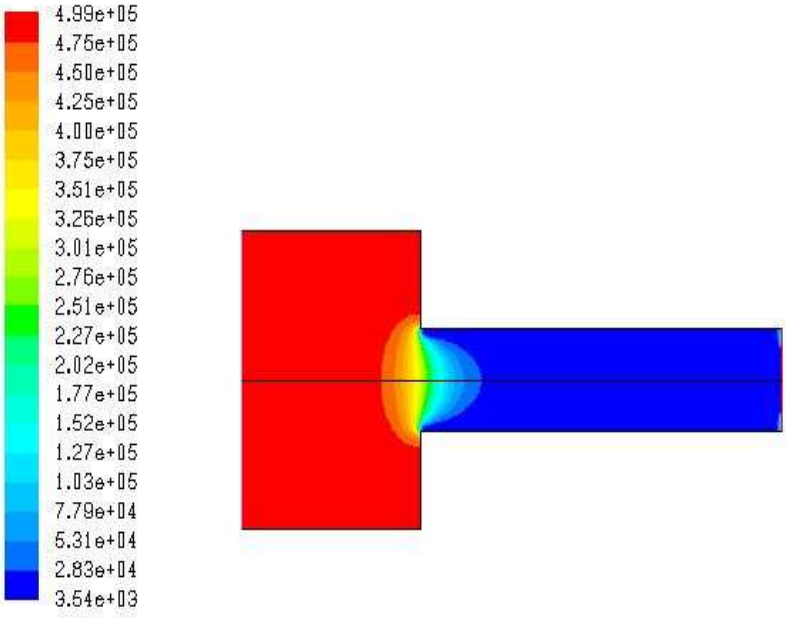

Figure 4-17: static pressure contour plot in a flow constriction

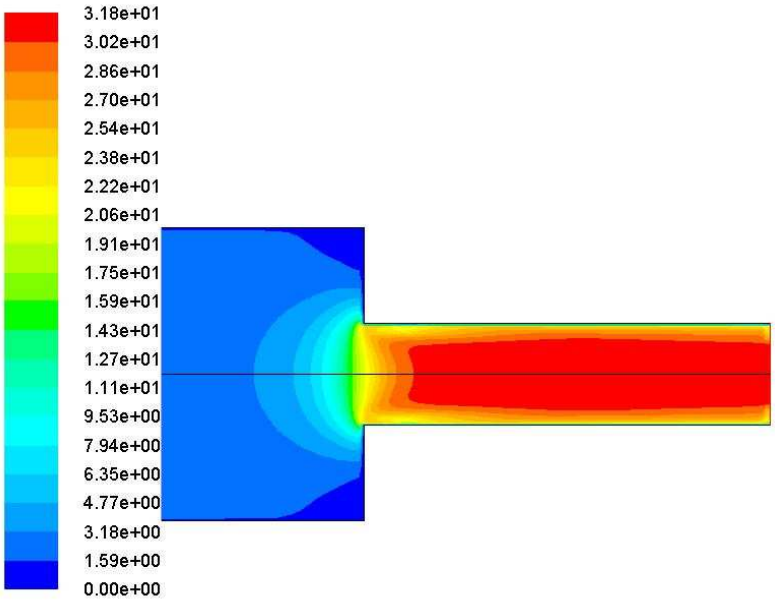

Figure 4-18: Contours of velocity magnitude in a flow constriction

The minimum static pressure predicted is the same as vapor pressure at operating temperature and pressure, which is 3540 Pa. The results confirm the prediction of cavitation and capability of the model we

used for our study. By analyzing the contour plot of turbulent kinetic energy (Figure 4-19), it is clear that, there exists a strong turbulent kinetic energy of 19 m^2/s^2, which can provide a significant amount of energy in the form of turbulent dissipation rate to support the energy requirement for cavitation.

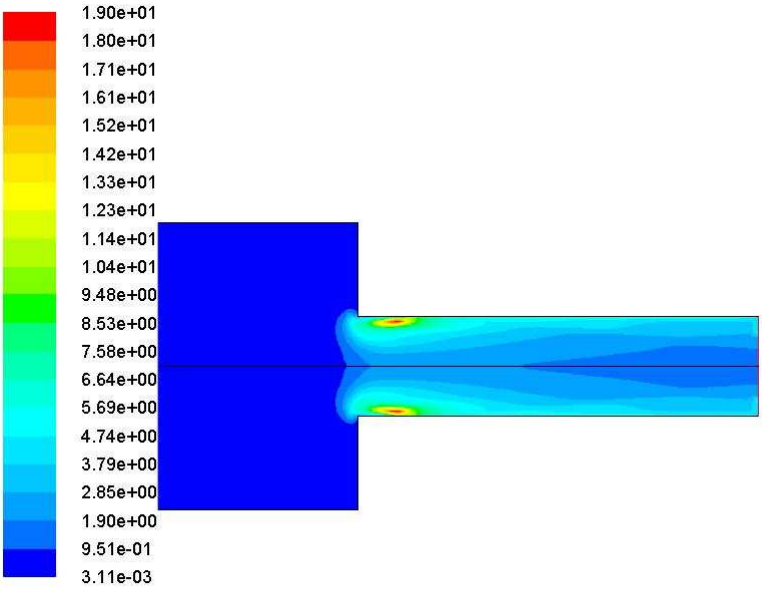

Figure 4-19: Contours of turbulent kinetic energy in a flow constriction with cavitation

4.2.2 Characterization of flow parameters on cavitation in a flow constriction

In order to understand the dependency of cavitation on flow parameters simulation is carried out at different flow velocities. For this, inlet pressure is varied from 3atm to 8atm gauge which gave average velocities at the outlet from 16m/s to 36.48m/s. In order to carry out

simulations at throat average velocities lower than 16m/s, the inlet velocity is varied as boundary condition. The inlet velocities are calculated using the equation 40.

$$A_i u_i = A_o u_o \qquad (40)$$

The predicted values are tabulated in Table 4-2.

Table 4-2: Study of cavitating flow through orifice

Avg. velocity at throat (m/s)	Static pressure (Pa)		Turb. Dissi. rate (m^2/m^3)	Vapor vol. fraction			cavitation number
	min	max		min	max	avg	
11.38	9386	197480	62563.35	0.0066	0.1808	0.0082	1.9
14.13	3856	238260	140781.7	0.0055	0.8032	0.0077	1.6
15	3540	293402	59656.73	0.0044	0.9996	0.0583	1.5
16	3540	299593	63373.46	0.0043	0.99	0.0606	1.4
22.98	3540	399472	112001.5	0	0.99	0.0612	1.3
27.52	3540	499355	171499.3	0.0026	0.9999	0.0609	1.2
31.02	3540	599237	256604.1	0.0022	0.9999	0.0606	1.2
33.89	3540	699120	373563.1	0.0019	0.9999	0.0605	1.2
36.48	3540	799005	483491.8	0.0016	0.9999	0.0604	1.1

At throat average axial velocities of 11.38 m/s and 14.13 m/s, the pressure did not reach vapor pressure and as a result there is no cavitation and the predicted average vapor volume fractions of 0.0082 and 0.0077 are from the dissolved gas present in the water. At a throat velocity of 15 m/s the pressure reached below vapor pressure (3540) and there is cavitation with an average vapor formation of 5%. This is in very good agreement with the experimental studies of Hu et al. [Hu et al., 1998] in a cavitation tube, where they reported a minimum throat velocity of 15.9 m/s for cavitation to occur. Cavitation number is calculated and it is found that

the cavitation inception number is 1.6. It is very close to the experimental results observed by Nurick [Nurick, 1976] where they observed cavitation inception number of 1.7. The maximum vapor formation is predicted at an average axial velocity of 22.98 m/s at throat and further increase in velocity did not change the amount of vapor formed by cavitation. The predicted results indicate that cavitation is a function of velocity, pressure drop and turbulent dissipation rate. This is in agreement with findings by Zhou and co-workers [Zhou et al., 1997] were they report an increase in fine particle flotation when the velocity of feed stream is increased through the cavitation tube. This clearly confirms the energy dependency of cavitation effects. However, above a certain velocity of 22 m/s at throat, the average vapor volume fraction remains almost constant, as shown in Figure 4-20 and further increase in flow velocity (or turbulent dissipation rate) does not increases average vapor volume fraction.

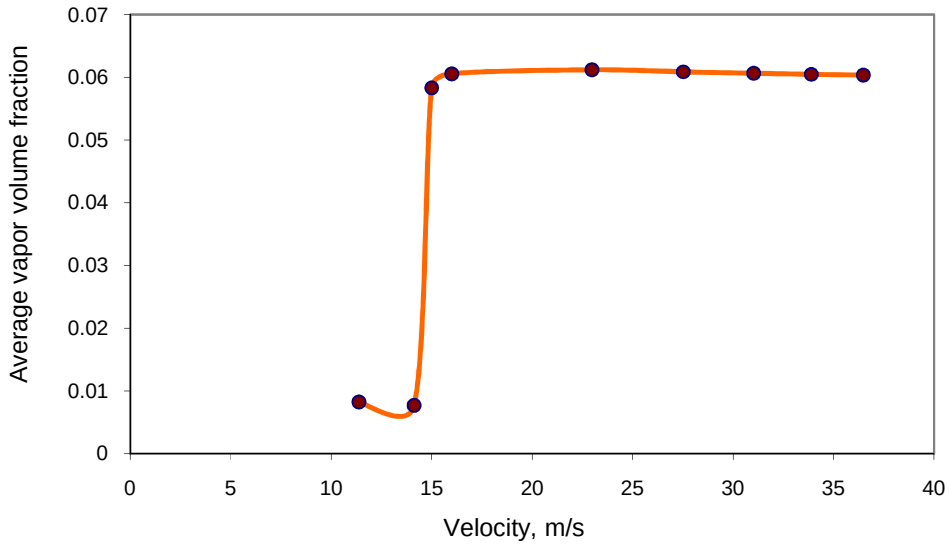

Figure 4-20: Plot of average vapor volume fraction vs. velocity in flow constriction

Once the cavitation reaches the saturation value of 0.06, further increase in velocity and kinetic energy is compensated with a steep increase in turbulent dissipation rate (Figure 4-21).

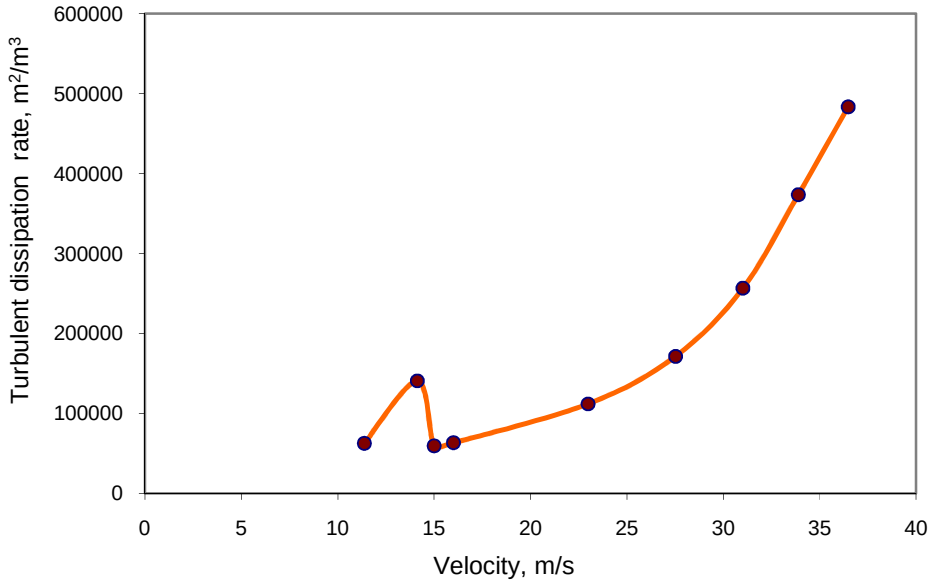

Figure 4-21: Plot of turbulent dissipation rate vs velocity in a flow constriction

The plot of minimum static pressure vs. velocity in flow constriction in Figure 4-22 indicates two regions: one is linear decreasing section and the other is constant static pressure of 3540 Pa, which is the vapor pressure at operating conditions. From this we can conclude that the initial cavitation before reaching vapor pressure is due to the presence of dissolved gas in the system. This dissolved gas can get released from the liquid state to the vapor state at high turbulence. The vapor volume fraction of 0.0082 at a minimum static pressure of 9386 Pa corresponds to

the total dissolved gas content which vaporized at high turbulence. Once the pressure reaches below 3540 Pa (vapor pressure), the volume fraction of vapor jumps to a value of 0.0583, which mainly constitutes of water vapor due to cavitation. Increasing throat velocity further did not change the minimum pressure, instead it increases the vapor volume fraction to 0.0612. If the velocity is increased further, it predicts a slight decrease in vapor volume fraction to 0.0606 and an increase in turbulent dissipation rate. This can be attributed to the increased collapsing of the cavities generated due to the increased turbulence in the system.

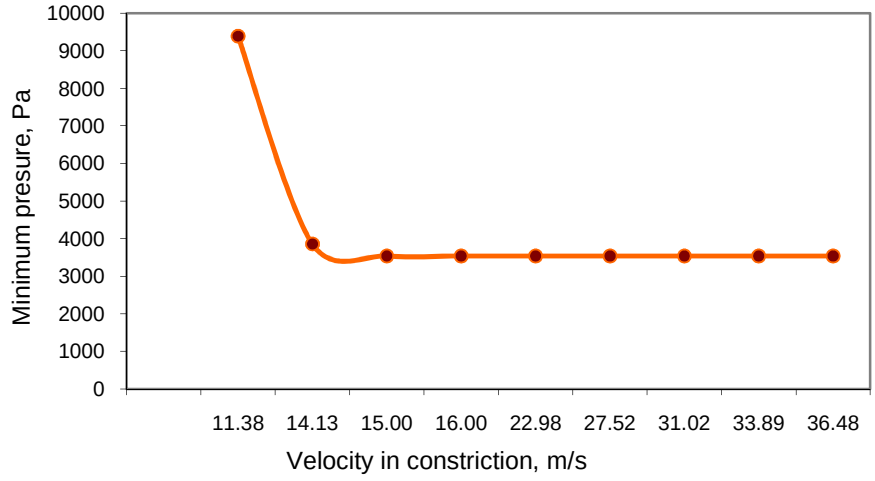

Figure 4-22: Plot of minimum static pressure reached vs. velocity in a flow constriction

4.2.3 Hydrodynamic cavitation in an HIA cell

Further simulations are carried out in the HIA cell for cavitating flow. A non-slip condition between vapor and liquid phase is assumed here as well. The input material properties are constant values at 20^{o}C and are summarized in Table 4-3 below.

Table 4-3: Material properties of the fluids (a) water-vapor, (b) water-liquid, and (c) air

(a) Material: water-vapor(fluid)

Property	Value	unit
Density	0.55419999	kg/m^3
Cp (Specific Heat)	2014	j/kg-k
Thermal Conductivity	0.0261	w/m-k
Viscosity	1.34E-05	kg/m-s
Molecular Weight	18.01534	kg/kg mol

(b) Material: water-liquid(fluid)

Property	Value	unit
Density	998.2	kg/m^3
Cp (Specific Heat)	4182	j/kg-k
Thermal Conductivity	0.6	w/m-k
Viscosity	1.00E-03	kg/m-s
Molecular Weight	18.01534	kg/kg mol

(c) Material: air (fluid)

Property	Value	unit
Density	1.225	kg/m^3
Cp (Specific Heat)	1006.43	j/kg-k
Thermal Conductivity	0.0242	w/m-k
Viscosity	1.79E-05	kg/m-s
Molecular Weight	28.966	kg/kg mol

Boundary conditions were set as impeller speed in RPM. Figures 4-23 and 4-24 shows the static pressure and vapor fraction contours obtained at 1500 RPM and a dissolved gas content of 15 ppm. With cavitation model on the pressure contour plot indicated static pressures lower than vapor pressure. This was in slight disagreement from the prediction on the orifice flow, where the minimum pressure obtained with cavitation model on was 3450 Pa, which is the vapor pressure of the system.

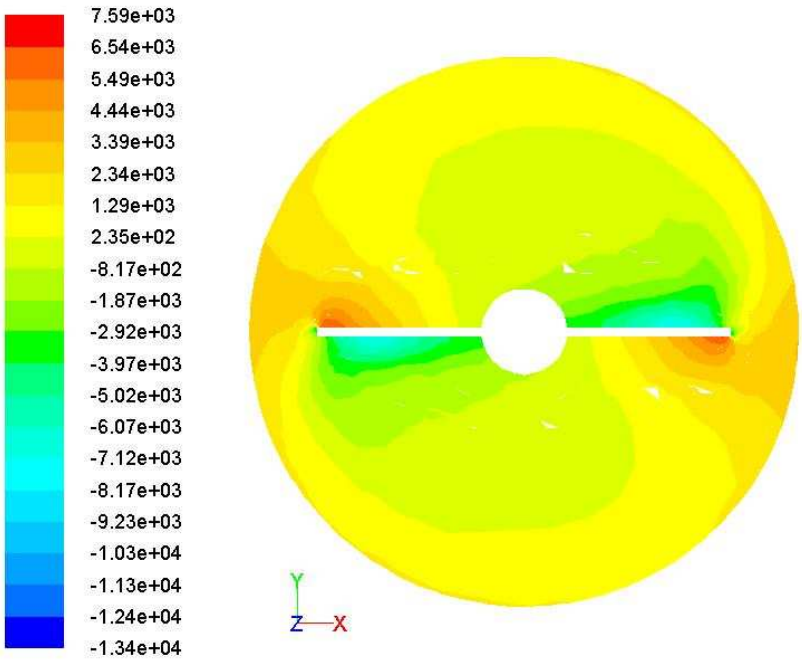

Figure 4-23: Static pressure contours in an HIA cell at impeller zone

As per equation 27, evaporation takes place when pressure P is lower than vapor pressure P_v and as such there should not be a pressure lower than the vapor pressure P_v. This clearly indicates the need for mesh

refinement of 3D geometry of HIA cell to capture the entire low pressure region to cavitation equation as in the 2-D model of orifice flow. In vapor fraction contour plot (Figure 4-24) lower pressure is found to be concentrated mainly behind the impellers. As a result the vapor formation is maximized behind the impellers where pressure is below vapor pressure.

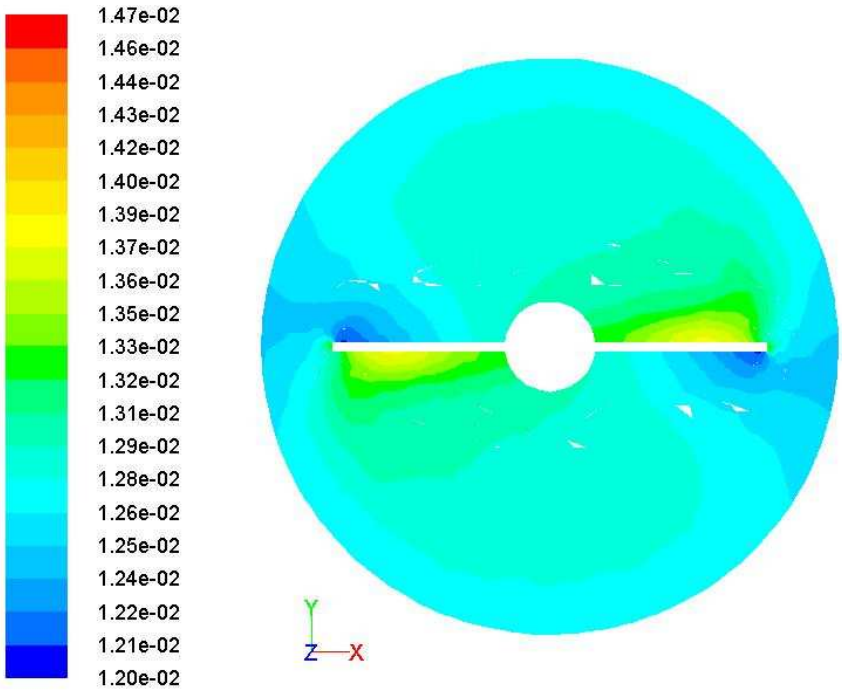

Figure 4-24: Vapor volume fraction contours in an HIA cell at impeller zone

A maximum vapor fraction of 0.01624 is predicted at the impeller zone with minimum gauge pressure of -20947 Pa and maximum velocity of 6.97 m/s at an impeller speed of 1500 RPM. The average volume

fraction of vapor in the system is predicted as to be 0.012703 as shown in Table 4-4.

Table 4-4: Shows dependency of vapor formation at different RPM

RPM	Maximum volume fraction of vapor predicted at impeller zone	Average Volume fraction predicted inside HIA cell
1500	0.01624	0.012703
2000	0.02066	0.012703
2500	0.02393	0.012703

When flow is simulated at 2500 RPM, maximum vapor fraction of 0.02393 is predicted at the impeller zone even though the average volume fraction in the whole system remains the same at 0.012703. The results obtained for cavitation at different RPM's are shown in Table 4-4. The increase in cavitation at impeller zone with increasing RPM indicates that cavitation is energy intensive. The increased vapor formation is due to the increased turbulent kinetic energy dissipation rate at higher RPM's.

In Figure 4-25 we can visualize the contours of turbulent kinetic energy at the impeller zone. The contour of velocity magnitude at the impeller zone is shown in Figure 4-26. These results are in good agreement with experimental observations of higher particle recovery at high feed velocity through a cavitating tube [Zhou et al., 1997].

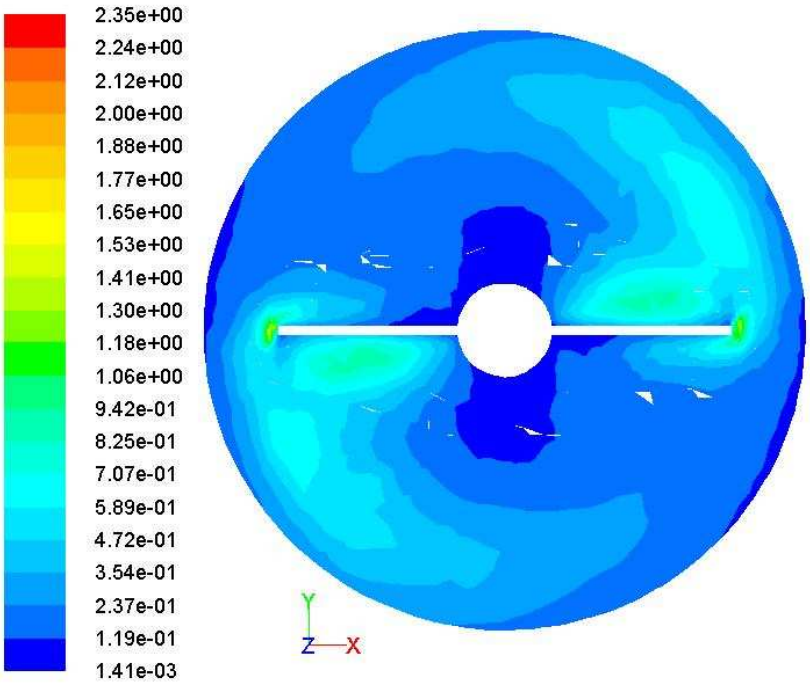

Figure 4-25: Contours of turbulent kinetic energy at impeller zone

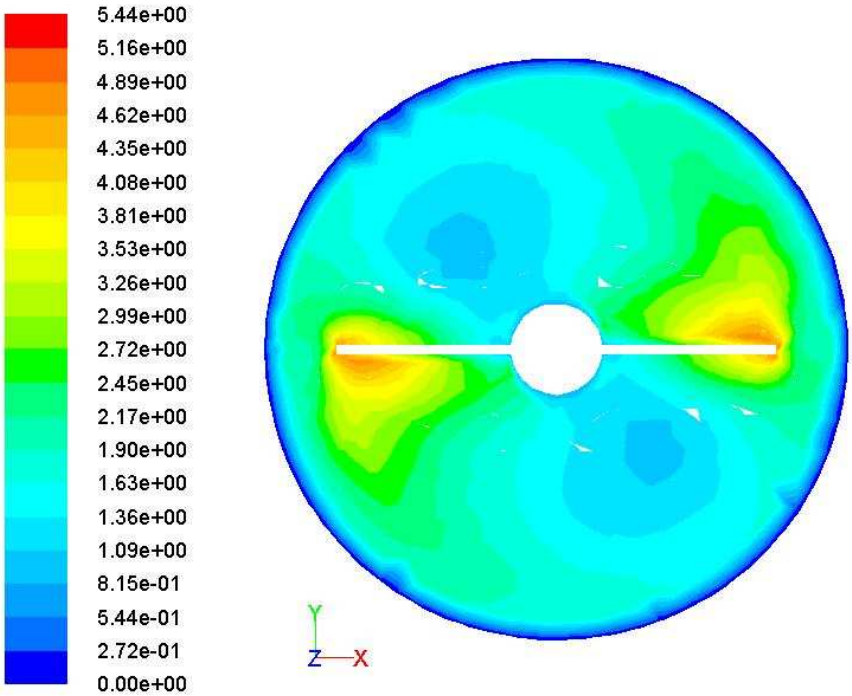

Figure 4-26: Contours of velocity magnitude at impeller zone

To study the effect of dissolved gas content on hydrodynamic cavitation, simulation is also carried out at 1500 RPM and different dissolved gas content of 50 ppm, 100 ppm and 200 ppm. The results are shown in Table 4-5. Figure 4-27 shows the volume fraction of vapor formed at 1500 RPM and different dissolved air content. Even though it is impossible for air to dissolve above 15 ppm in water at normal temperature and pressure, CO_2 can be dissolved in water up to 600 ppm [Dalmolin et al., 2005]. It is found that amount of vapor predicted (average volume fraction) varies linearly with dissolved gas content. In fact, the cavitated vapor predicted constitutes of both dissolved gas and water vapor.

Table 4-5: Comparison of amount of vapor formed by cavitation and by dissolved air in the liquid at 1500 RPM

Dissolved Gas Content in liquid, ppm	Volume fraction of dissolved gas content in vapor state.	Average volume fraction of cavitated vapor phase predicted by Fluent	Difference
15	0.01209	0.0127	0.00061
50	0.03921	0.0415	0.00229
100	0.07547	0.0794	0.00393
200	0.14035	0.1472	0.00685

This observation clearly raises the question whether the vapor phases have any water vapor in it or just the noncondensable gases. In order to understand this, the volume fraction of noncondensable gas content is calculated from ppm and compared with the average volume fraction of vapor.

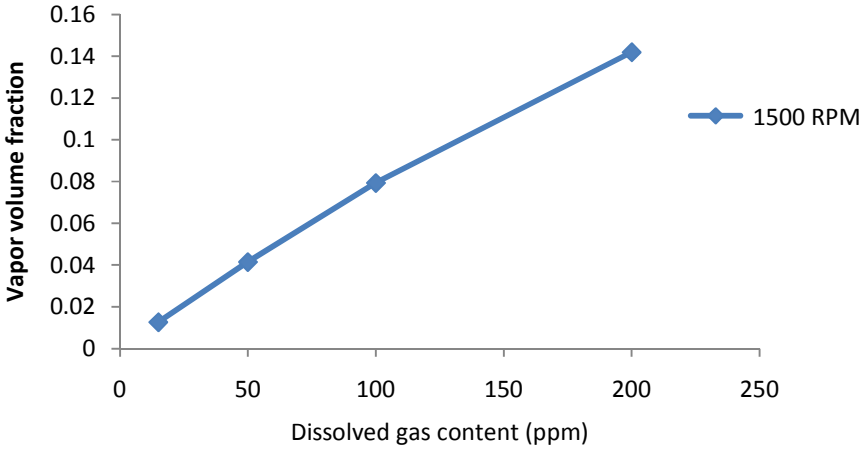

Figure 4-27: Volume fraction of vapor formed at different dissolved air content

To understand how much vapor actually formed by cavitation the volume fraction of dissolved gas (Φ_g) at vapor state can be calculated from the densities as given by

$$\Phi_g = \frac{f_g/\rho_g}{f_g/\rho_g + (1 - f_g)/\rho_l} \qquad (41)$$

where $f_g$is the noncondensable mass fraction, ρ_g is the noncondensable gas density and ρ_l is the liquid density. The volume fraction of dissolved gas Φ_g, is calculated at different noncondensable gas concentration and tabulated in Table 4-5. At 15 ppm the volume fraction of noncondensable gases is 0.01209 which is approximately the same as the average volume fraction of vapor predicted by simulation at 15 ppm noncondensable gas content, irrespective of RPM. The difference between the predicted vapor fraction and the dissolved gas fraction shows a slight increase with dissolve gas content in the water, indicating that presence of dissolved gas increases cavitation. This slight increase in the amount of vapor

predicted with the increase in dissolved gas content is attributed to easy cavitation with dissolved gases which act as weak spots for cavitation.

One of the interesting observations found was that the average volume fraction of vapor remained constant irrespective of RPM and increased with increasing noncondensable gas concentration as shown in Table 4-4. Considering the fact that the simulation was at steady state and the cavitation module used contains both evaporation and condensation terms in it, the nature of average volume fraction to be the same for all RPM's can be justified. Once the vapor formed at impeller zone passes through the high pressure zone of bulk region, it can get condensed and thus can reduce the average vapor volume fraction within the HIA cell to be the same as the volume fraction of noncondensable gas in the mixture. But at impeller zone a higher volume fraction of 0.0164 is predicted, which indicates the cavitation effect at impeller zone. An increase in vapor volume fraction with RPM at constant dissolved gas content at impeller zone indicated formation of cavitation vapor in the HIA cell. Because, at 1500 RPM the vapor fraction predicted was more than the volume fraction of 15 ppm of dissolved gas content as illustrated in Table 4-5. Further increase in vapor fraction with RPM indicates that it is merely the cavitated vapor that contributes towards this increase. This clearly confirms the role of energy input in cavitation in a HIA cell. Amount of vapor formed was less in an HIA cell than in an orifice. This discrepancy can be due to the much higher pressure drop in the orifice than in the mixing tank operating

at atmospheric pressure. Further quantitative improvements are to be expected by introducing finer mesh with hexahedral elements [song et al., 2009].

4.3 Population balance study on orifice flow

Population balance simulations are conducted using discrete methods of solution, which gives a bubble size distribution directly. This method requires specifying the range of bubble sizes with span not more than two or three orders of magnitude. The bubble breakage frequency and aggregation frequency is calculated using Luo model in ANSYS Fluent. The Population Balance model uses different methods of mass transfer functions to calculate phase changes. Unfortunately cavitation mass transfer model is not included. We coupled a user defined function (UDF) to produce cavitation mass transfer between phases when population balance model is on. Using discrete method, UDF with a nucleation radius of 2 microns is simulated.

Geometric ratio is kept as 2 with a minimum size of 2 microns and 10 bins. The contours (Figure 4-28, 4-29, 4-30, 4-31 and 4-32) of bin sizes showed that smaller size bubbles are present at the beginning of the throat. That is 2 microns at the beginning and 128 microns towards the end of the throat (Figure 4-28 and 4-29). There were not any bubbles of this size range predicted on the flow separation area right after the throat entrance where cavitation predicted was 100%.

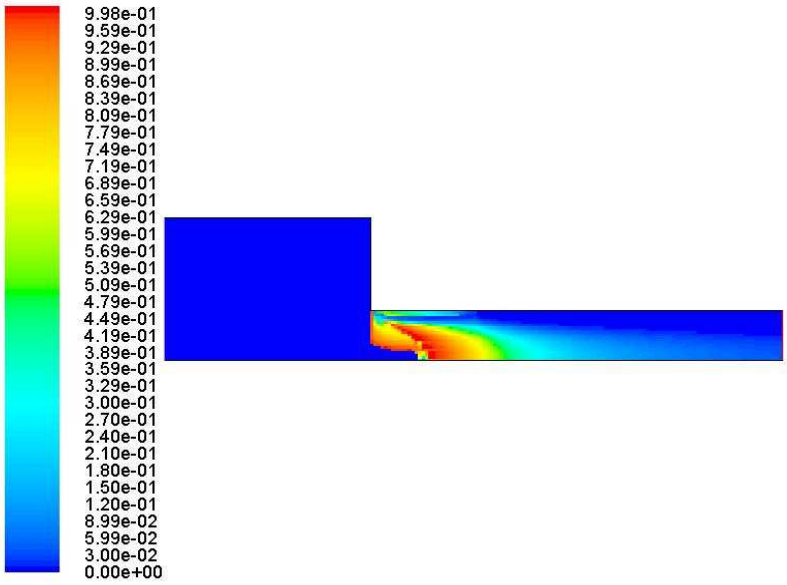

Figure 4-28: Contours of 2 micron size bubbles

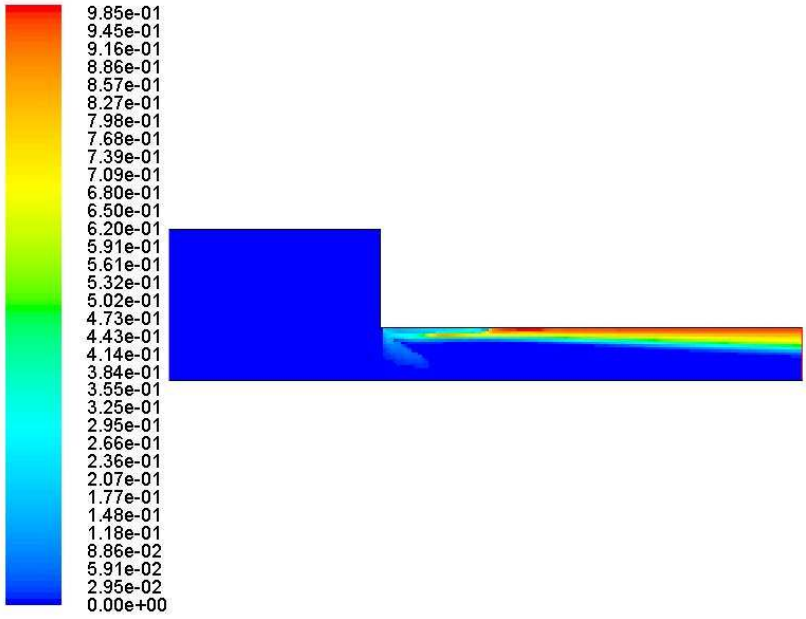

Figure 4-29: Contours of 128 micron size bubbles

This observation confirms that smaller bubbles are present at turbulent zone and then these bubbles aggregate to form large bubbles on

areas close to wall and farther downstream. In order to understand the possible occurrence of nano-size bubbles, simulation was performed with a size range of 20 nm to 1200 nm. The contour plot in Figure 4-30 shows that there were only few bubbles of size 1.28 microns. In Figure 4-31, bubbles of size 30 nm are predicted at the flow separation region (right after the throat entrance) where maximum cavitation volume fraction was predicted. Bubbles of size 20 nm were predicted to present in the centre part of the throat as shown in Figure 4-32, where turbulence was very high. This indicates presence of high breakage rate in the system due to turbulence and a possibility for nano-sized bubbles to exist in such an environment of turbulence and fluid properties. The presence of nano-bubbles supports the mechanism of in-situ bubble formation by hydrodynamic cavitation on hydrophobic particles, which then helps the fine particles to aggregate.

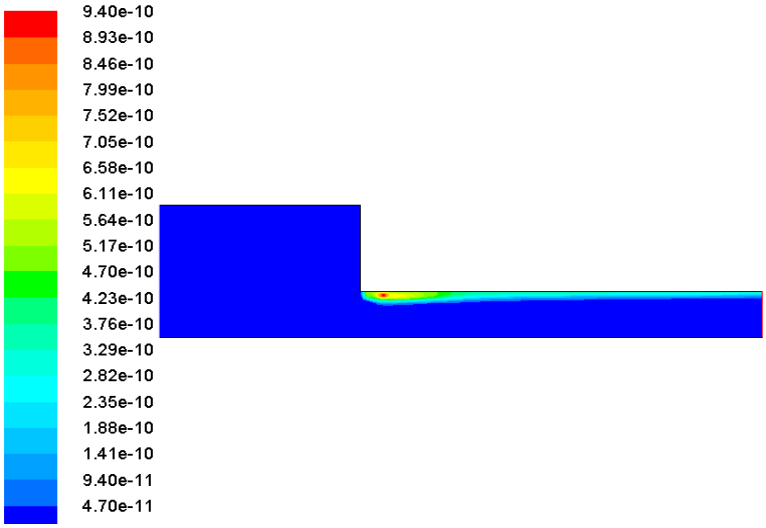

Figure 4-30: Contours of 1.28 micron size bubbles

When simulations are carried out at size range greater than two orders of magnitude, solution diverged. This finding suggests that PB module can handle only two order of magnitude of size range in discrete method of solution. Then simulations are carried out at different size ranges of two orders of magnitude. The results showed that the size range is limited to 20 nm to 200 microns. If the size were reduced below 20 nm, the solution showed that the bins are empty. For bubble sizes above 200 microns, the solution showed instability with highly fluctuating residuals.

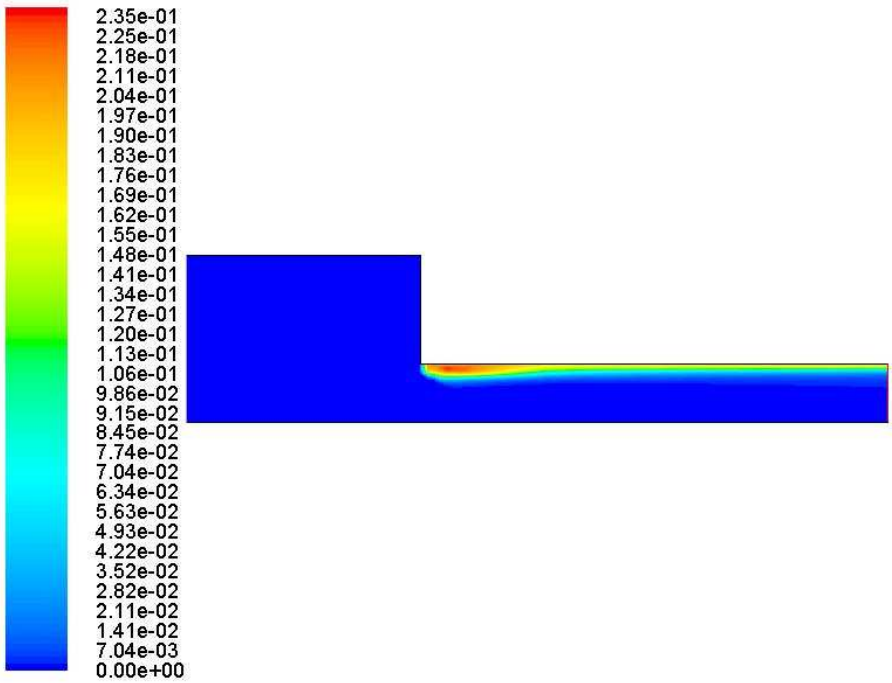

Figure 4-31: Contours of 30 nm size bubbles

The population balance model predicted that the size range can be between 20 nm to 200 microns approximately. Experimental work by Tao et al. [Tao et al., 2008] to obtain bubble size distribution of cavitated bubbles in a picobubble generator (cavitation tube) using a Cillas 1064

laser particle size analyser reported presence of 40 nm to 200µm bubbles with a mean size of 900nm bubbles. Considering the fact that the measurement range of the instrument used is from 40 nm to 500 microns, one cannot rule out the possibility of presence of bubbles less than 40nm.

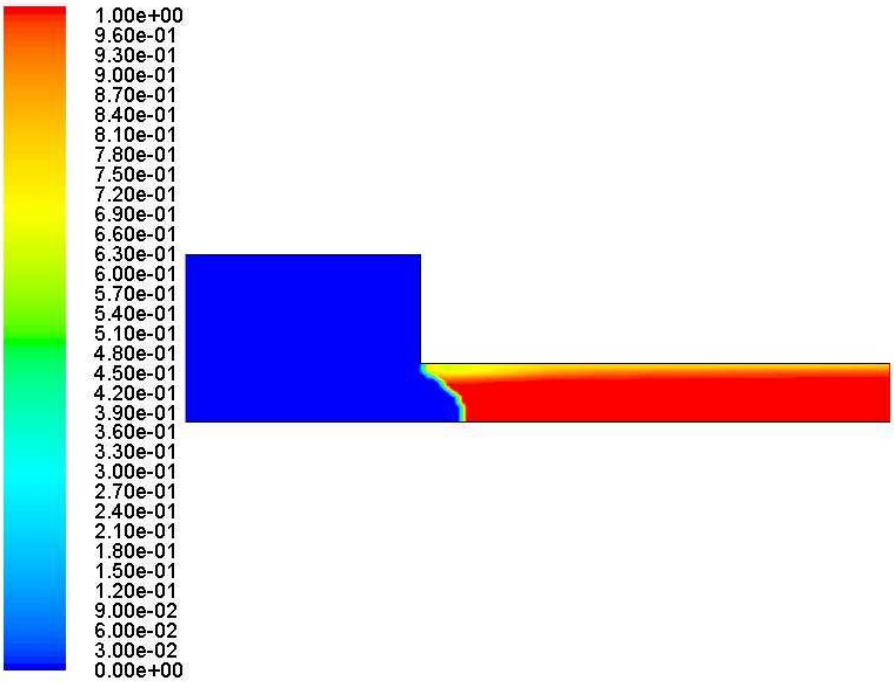

Figure 4-32: Contours of 20 nm size bubbles

Table 4-6: Number Density for Discrete Method (20 nm to 1200 nm)

Particle Diameter , m	**Number Density,** #/m^3
1.28E-06	25.684315
8.06E-07	5390.9346
5.08E-07	774347.19
3.20E-07	74131360
2.02E-07	4.58E+09
1.27E-07	1.76E+11
8.00E-08	4.09E+12
5.04E-08	5.99E+13
3.17E-08	6.40E+14
2.00E-08	1.50E+16

Surface average number density function for 20 nm to 1200 nm size range is shown in Figure 4-33. This shows that maximum number density is for particles with 20 nm size, which are 1.50E+16. For 128 micron particles, the maximum number density was about 2.04E+10. Table 4-6 shows the number density per bin for 20 nm to 1200 nm size range simulation.

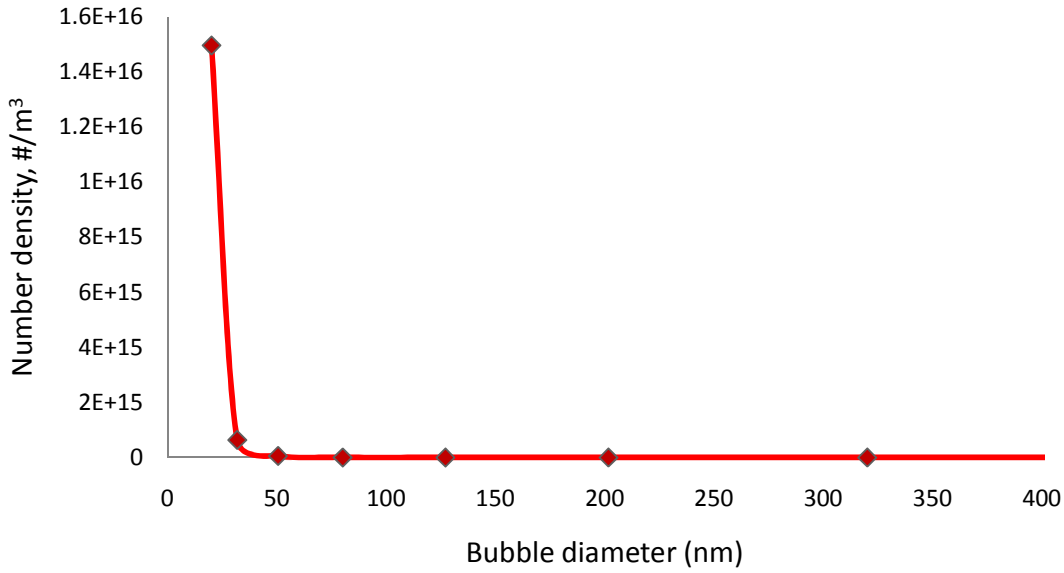

Figure 4-33: Bubble number density plot for 20 nm to 1200 nm size simulation

Further study is needed to obtain the actual size range of bubbles in a flow through constriction. Once a size range is obtained, this model can very well predict the size distribution taking in to account the aggregation and breakage rate in the system.

The hydrodynamics in a flow through constriction and an HIA cell is successfully studied using CFD modelling. Modelling results for cavitation in a flow constriction demonstrate good agreement with experimental

values in literature. Population Balance module predicted bubble size range as observed in laboratory tests. The vapor volume fraction in a HIA cell showed dependence on impeller speed and the pressure drop as expected, indicating cavitation is energy intensive in HIA cell. In general, CFD modelling can provide insight in to the flow properties in HIA cell and provide information required for future scale up of high intensity agitation systems.

Chapter 5: Conclusions

CFD modelling of a high intensity agitation cell is performed to understand flow patterns in it with various types of impellers. Distributions of various flow parameters such as velocity, static pressure, turbulent dissipation rate and turbulent kinetic energy were obtained and compared for potential cavitation generation different impeller types. Among all the impellers studied, straight 4-vane impeller predicted the maximum velocity and kinetic energy, and minimum static pressure.

Cavitation modeling is performed for a flow constriction and it predicted strong cavitation near throat area and considerable amount of cavitated vapour formed in it. The minimum velocity required for cavitation to occur is obtained as 15 m/s, which is in good agreement with the experimental data in literature [Hu et al., 1998]. This also corresponds to a cavitation inception number of 1.6 which is very close to the value reported in the literature [Nurick, 1976]. Cavitated vapour volume fraction increased with increasing throat velocity and reached a maximum. Further increase in velocity did not increase the cavitation, instead turbulent dissipation rate increased drastically. This is in agreement with findings by Zhou and co-workers [Zhou et al., 1997] where they reported an increase in fine particle flotation when the velocity of feed stream is increased through the cavitation tube. This clearly confirms the energy dependency of cavitation effects.

Simulation of hydrodynamic cavitation in an HIA cell is performed at different impeller speeds and with different dissolved air content. It is found that the amount of vapour formation increases with impeller speed and dissolved air content. These results predicted are qualitatively in good agreement with experimental observations. Further quantitative improvements are to be expected by introducing finer mesh with hexahedral elements [song et al., 2009].

The population balance model was explored for orifice flow, successfully establishing the bubble size range, exploring model stability, and providing appropriate number density functions at the outlet. The model predicted the existence of nano-sized bubbles in the system and the bubble size distribution obtained was comparable with experimental data in literature [Tao et al., 2008]. Despite cavitation model implementation difficulties, cavitating (evaporating) flow was implemented into the population balance model using a UDF as the nucleation term. The population balance provided an appropriate number density function at the outlet of the orifice. Further work is needed to include the condensation rate term into population balance model. It is hypothesized that this may be possible to implement by modifying the growth term or the breakage function in the balance equations.

Chapter 6: Problems Faced

Two dimensional (2D) flow simulations of orifice flow were not computationally tedious task and it can be performed very fast and predicted an expected amount of vapour formation in it. When the cavitation model was enabled, it converted all the regions of pressures lower than vapour pressure to cavitation, and as a result the minimum pressure predicted in the system was 3450 Pa, which is the vapour pressure (Figure 4-17). On the other hand, the three dimensional (3D) simulation in an HIA cell could not predict an expected amount of vapour formation. In addition, it predicted pressures lower than vapour pressure with cavitation model on (Figure 4-23) which is not in agreement as per equation 27, which says that, whenever pressure is lower than vapour pressure there is vapour formation by cavitation effect. This indicates need for further mesh refinement or use of hexahedral elements at impeller zone to predict more cavitation. Song et al. reported similar problem of less gas volume fraction predicted in a flotation cell when simulation is carried out with a tetrahedral mesh. When a hexahedral mesh is used [Koh et al., 2003, Lane et al., 2005] results were in good agreement with experimental values. This required prolonged computation time and speed and due to time constraint this is not clarified in this study.

Chapter 7: Scope of Future Work

1) The 3D mesh of HIA cell can be refined further to obtain more appropriate quantitative results of cavitation vapour formation. Hexahedral elements can be tried to obtain more vapour formation as reported in literature.

2) Modelling cavitation for different impeller types such as radial disc, pitched blade and flat 4-vane impeller, can be done to understand the energy intensive nature of cavitation. In fact, the impeller characterization study predicted a high turbulent dissipation in a 4-vane straight impeller HIA cell.

3) Implement condensation term to UDF of cavitation model for population balance modeling to obtain more realistic results since vaporization and condensation occur simultaneously in a real system.

4) The current study limits to population balance study in a 2D model flow constriction, and it can be performed to obtain population balance results in an HIA cell.

5) Experimental studies can be done to validate the bubble size distribution range in an orifice flow and in an HIA cell.

References

1. Arndt, R. E. A., “Cavitation in fluid machinery and hydraulic structures”, *Ann. Rev. Fluid Mech*., vol. 13, pp. 273-328, 1981.
2. Aschenbrenner, T., “Classification of vortex and cavitation phenomena and assessment of CFD prediction capabilities”, *Proceedings of the 23rd IAHR Symposium on Hydraulic Machinery and Systems*, IAHR, Yokohama, Japan, 2006.
3. Athavale, M. M., Li, H.Y., Jiang, Y.U., Singhal, A.K., “Application of the full cavitation model to pumps and inducers”, *International Journal of Rotating Machinery*, vol. 8, no. 1, pp. 45-56, 2002.
4. Batchelor, G.K., “An Introduction to Fluid Dynamics*”, Cambridge Univ. Press*, Cambridge, England, 1967.
5. Brennen, C. E., “Cavitation and bubble dynamics”, *Oxford University Press*, Oxford, 1995.
6. Bulatovic S. M., Salter R. S. H., “High intensity conditioning: a new approach to improve flotation of mineral slimes”, *Proceedings of Conference of Metallurgists*, Halifax, Canada, pp. 182-197, 1989.
7. Dalmolin, I., kovroinski, E., Biasi, A., Corassa, M. L., Dariva, C., and Oliveria, J. V., “Solubility of carbon dioxide in binary and ternary mixtures with ethanol and water”, *Fluid Phase Equilibria*, vol. 245, no: 2, pp. 193-200, 2005.
8. Ding, H., Visser, F. C., Jiang, Y., Furmanczyk, M., “Demonstration and validation of a 3D CFD simulation tool predicting pump performance and cavitation for industrial applications”, *Proceedings of the ASME Fluids Engineering Division Summer Conference*, Colorado, pp. 277-293, 2009.
9. Fukaya, M., Tamura, Y., Matsumoto, Y., “Prediction of cavitation intensity and erosion area in centrifugal pump by using cavitating flow simulation with bubble flow model”, *Nihon Kikai Gakkai*

Ronbunshu, B Hen/Transactions of the Japan Society of Mechanical Engineers, Part B, vol. 74, no.10, pp. 2116-2123, 2008.

10. Hu, H., Zhou, Z., Xu, Z., Finch, J. A., “Numerical and experimental study of a hydrodynamic cavitation tube”, *Metallurgical and Materials Transactions B: Process Metallurgy and Materials Processing Science*, vol. 29, no. 4, pp. 911-917, 1998.
11. Koh, P. T. L., Schwarz, M. P., Zhu, Y., Bourke, P., Peaker, R., and Franzidis, J. P., “Development of CFD models of mineral flotation cells,” *Third International Conference on CFD in the Minerals and Process Industries, CSIRO*, Melbourne, Australia, pp. 10-12, December 2003.
12. Kuiper, G., “Cavitation research and ship propeller design,” *Applied Scientific Research*, vol. 58, no. 1-4, pp. 33–50, 1998.
13. Lane, G. L., Schwarz, M. P., Evans, G. M., “Numerical modelling of gas-liquid flow in stirred tanks”, *Chemical Engineering Science 60 (8-9 SPEC. ISS.)*, pp. 2203-2214, 2005.
14. Li, S., Liu, S., Zhang, L., Wu, Y., “A mixture model with modified mass transfer expression for cavitating turbulent flow simulation”, *Engineering Computations (Swansea, Wales)*, vol. 25, no. 4, pp. 290-304, 2008.
15. Miettinen, T., Ralston, J., and Fornasiero, D., “The limits of fine particle flotation,” *Minerals Engineering*, vol. 23, no. 5, pp. 420-437, 2010.
16. Nurick. W.H, “Orifice cavitation and its effect on spary mixing” ASME J. *Fluids Eng*, 98, pp 681-687, 1976.
17. Rubio J., “Conditioning effects on flotation of a finely divided non sulphide copper ore”, *Trans Metall*, pp. 87-107, 1978.
18. Singhal, A. K., Li, H. Y., Athavale, H. H., and Jiang, Y., “Mathematical basis and validation of the full cavitation model, ” *Journal of Fluids Engineering,* vol. 124, no. 3, pp. 617-614, 2002.

19. Song, T., Zhou, J. W., and Shen, Z. C., “CFD simulation of gas-liquid flow in a large scale flotation cell,” *Seventh International Conference on CFD in the Minerals and Process Industries CSIRO,* Melbourne, Australia, 9-11, December 2009.
20. Susan-Resiga, R.F., Muntean, S. and Anton, J., “Numerical analysis of cavitation inception in Francis turbine”, Proceedings of the XXIst IAHR Symposium on Hydraulic Machinery and Systems, IAHR, Lausanne, 2002.
21. Tao, D., Yu, S., Zhou, X., Honaker, R. Q., Parekh, B. K., “Picobubble column flotation of fine coal”, *International Journal of Coal Preparation and Utilization*, vol. 28, no. 1, pp. 1-14, 2008.
22. Tao, Y., Liu, J., Yu, S., Tao, D., “Picobubble enhanced fine coal flotation”, *Separation Science and Technology*, vol. 41, no. 16, pp. 3597-3607, 2006.
23. Theory guide, ANSYS Fluent 12.0, *ANSYS Inc* , April 2009
24. Trahar, W. J., and Warren, L. J., “The floatability of very fine particles – A review,” *International Journal of Mineral Processing*, vol. 3, no. 2, pp. 103-131, 1976.
25. Warren, L. J.,”Shear-flocculation of ultraline scheelite in sodium oleate solutions”, *Colloid Interface Sci*, vol. 50, pp. 307-318, 1975.
26. Wei, S., Yue-hua, H., Jing-ping, D., Run-qing, L., “Observation of fine particle aggregating behavior induced by high intensity conditioning using high speed CCD”, *Trans. Nonferrous Met. SOC China*, vol. 16, pp. 198-202, 2006.
27. Zhou, Z. A., Xu, Z. H., and Finch, J. A., “Role of hydrodynamic cavitation in fine particle flotation,” *International Journal of Mineral Processing*, vol. 51, no. 1-4, pp. 139-149, 1997.
28. Zhou, Z. A., Xu, Z., and Finch, J. A., “Fundamental study of cavitation in flotation” *In: Proceedings of the 19th International Mineral Processing Congress*, San, Francisco, vol. 3, pp. 93-97, 1995b.

29. Zhou, Z. A., Xu, Z., and Finch, J. A., “On the role of cavitation in particle collection during flotation – a critical review”. *Minerals Engineering*, vol. 15, no. 7, 1073-1084, 1994.
30. Zhou, Z. A., Xu, Z., Finch, J.A., Masliyah, J. and Chow, R.S., “On the role of cavitation in particle collection in flotation – a critical review. II,” *Minerals Engineering,* vol.22, no. 5, pp. 419-433, 2009.
31. Zima, P., et al., “Bubble creation in water with dissolved gas: Prediction of regions endangered by cavitation erosion”, *Proceedings of 14th International Conference on the properties of water and steam (ICPWS),* Kyoto, pp. 232-235, 2004.
32. Zwart, P. J., “Numerical Modelling of Free Surface and Cavitating Flows”, *VKI Lecture Series*, 2005.

Appendix -A: Cavitation (Evaporation) UDF

```
/************************************************************************
UDF that computes the particle nucleation rate
************************************************************************/
#include "udf.h"
#include "sg_pb.h"
#include "sg_mphase.h"

 DEFINE_PB_NUCLEATION_RATE(cavnuc_rate, cell, thread)
{
  real J,SS,CR,CK,P,p_oper,dp,dp0;
  real Kn = 4.0e10; /* nucleation rate constant */
  real T, Jn;
  real rhoV, rhoL;
  real p_vapour=3400;
  real source,mass_dotV, mass_dotL;
  real Diam=1e-9, pi=3.14;
  Thread *tc = THREAD_SUPER_THREAD(thread); /* obtain mixture thread */
  Thread **pt = THREAD_SUB_THREADS(tc);     /* pointer to sub_threads */
  Thread *tp = pt[P_PHASE];                 /* primary phase thread */
  CR=C_R(cell,thread);
  CK=C_K(cell,thread);
  P=C_P(cell,thread);
  p_vapour += MIN(0.195*C_R(cell,thread)*C_K(cell,thread), 5.0*p_vapour);
  p_oper = RP_Get_Real("operating-pressure");
  dp = p_vapour - ABS_P(P,p_oper);
  rhoV = 0.02;   /* density of vapour */
  rhoL = 1000.0; /* density of water */

  dp0 = MAX(0.1, ABS(dp));
  source = sqrt(2.0/3.0*rhoL)*dp0;
  mass_dotV = rhoV*source;
  mass_dotL = rhoL*source;

  Jn=mass_dotV/rhoV/(4/3*pi*pow(Diam,3));

/*
    if (dp>0)
      printf( "Jn:  %f\n", Jn);
*/
```

```
 if (dp>0)
     {
       J = MIN(Jn,1e20);
     }
   else
     {
       J = 0.0;
     }
   return J;
}
```